JGR Space Physics

RESEARCH ARTICLE
10.1029/2023JA031607

New Chorus Diffusion Coefficients for Radiation Belt Modeling

Jin-Mann Wong[1], Nigel P. Meredith[1], Richard B. Horne[1], Sarah A. Glauert[1], and Johnathan P. J. Ross[1]

[1]British Antarctic Survey, Natural Environment Research Council, Cambridge, UK

Key Points:

- Chorus diffusion rates mainly ruled by small wave normal angles (WNA) but for 4 < MLT < 11 high WNAs can dominate pitch angle diffusion
- Choice of external magnetic field model between TS04 and OP77Q can have significant impact on the chorus diffusion coefficients at lower L^*
- New chorus diffusion rates at low L^* during active conditions primarily larger than two existing diffusion matrices by up to a factor of 10

Correspondence to:
J.-M. Wong,
jinmannwong@gmail.com

Citation:
Wong, J.-M., Meredith, N. P., Horne, R. B., Glauert, S. A., & Ross, J. P. J. (2024). New chorus diffusion coefficients for radiation belt modeling. *Journal of Geophysical Research: Space Physics*, *129*, e2023JA031607. https://doi.org/10.1029/2023JA031607

Received 19 APR 2023
Accepted 1 OCT 2023

Abstract Whistler mode chorus is an important magnetospheric wave emission playing a major role in radiation belt dynamics, where it contributes to both the acceleration and loss of relativistic electrons. In this study we compute bounce and drift averaged chorus diffusion coefficients for 3.0 < L^* < 6.0, using the TS04 external magnetic field model, taking into account co-located near-equatorial measurements of the wave intensity and f_{pe}/f_{ce}, by combining the Van Allen probes measurements with data from a multi-satellite VLF wave database. The variation of chorus wave normal angle (WNA) with spatial location and f_{pe}/f_{ce} is also taken into account. We find that chorus propagating at small WNAs has the dominant contribution to the diffusion rates in most MLT sectors. However, in the region 4 ≤ MLT < 11 high WNAs dominate at intermediate pitch angles. In the region 3 < L^* < 4, the bounce and drift averaged pitch angle and energy diffusion rates during active conditions are primarily larger than those in our earlier models by up to a factor of 10 depending on energy and pitch angle. Further out, the results are similar. We find that the bounce and drift averaged energy and pitch angle diffusion rates can be significantly larger than the new model in regions of low f_{pe}/f_{ce}^{eq}, where the differences can be up to a factor of 10 depending on energy and pitch angle.

Plain Language Summary Relativistic electrons in the Earth's outer radiation belt are a significant space weather hazard. The belt, which lies at altitudes from 13,000 to 40,000 km in the Earth's magnetic equatorial plane, is highly dynamic with fluxes of relativistic electrons varying by orders of magnitude on timescales ranging from minutes to months. This variability is controlled by a variety of transport, acceleration and loss processes. One particularly important process is the interaction with a plasma wave, known as chorus. These waves play a significant role in both the acceleration and loss of energetic electrons. In this study we derive new diffusion rates for these interactions and find that the rates can exceed those in our earlier models by up to a factor of 10. The new diffusion rates will be incorporated into the British Antarctic Survey Radiation Belt Model to produce better space weather models and forecasts.

1. Introduction

The Earth's radiation belts were discovered over 60 years ago, at the beginning of the space age (Van Allen, 1959; Van Allen & Frank, 1959), but many questions remain regarding the relative importance of the physical processes governing their variability. The inner radiation belt, which lies at geocentric distances of 1.1–2.0 R_E in the Earth's magnetic equatorial plane, is relatively stable, except during the largest geomagnetic storms (Baker et al., 2007). However, the outer radiation belt, which typically lies at geocentric distances of 3–8 R_E in the Earth's magnetic equatorial plane, is highly variable. Here, the flux of MeV electrons can change by several orders of magnitude on timescales ranging from minutes to weeks or even longer (Baker et al., 1994).

Understanding the variability of these relativistic electrons is important since enhanced fluxes can damage satellites (Koons & Fennel, 2006) and pose a risk to humans in space. Wave-particle interactions are known to play a fundamental role in the dynamics of the belts (Thorne, 2010), although their precise roles are yet to be determined. One very important wave mode that significantly affects the dynamics of energetic electrons in the outer radiation belt is chorus, so-called because, when converted to sound, it often resembles bird song in the dawn chorus.

Chorus is a naturally occurring whistler mode emission that typically occurs in short, 0.1 s, relatively coherent and repetitive bursts, with rising or, less often, falling tones at frequencies below the local electron gyrofrequency f_{ce} (Li et al., 2012; Santolík et al., 2004; Tsurutani & Smith, 1977). The waves are generated outside of the plasmapause by suprathermal electrons injected into the inner magnetosphere during storms and substorms

(Li et al., 2010; Omura et al., 2008). Consequently chorus is substorm-dependent with the largest intensities being seen outside the plasmapause from 21 MLT through dawn to noon during active conditions (Agapitov et al., 2018; Li et al., 2009; Meredith et al., 2001; Miyoshi et al., 2013). The waves often have a power gap at $0.5f_{ce}$, which separates the emissions into so called lower band, $0.1f_{ce} < f < 0.5f_{ce}$, and upper band, $0.5f_{ce} < f < f_{ce}$, chorus (Koons & Roeder, 1990; Tsurutani & Smith, 1977).

Gyroresonant wave-particle interactions with chorus play a major role in radiation belt dynamics contributing to both the acceleration and loss of relativistic electrons (Bortnik & Thorne, 2007). For example, chorus waves are thought to be largely responsible for the gradual build up of radiation belt electrons that occur during the recovery phase of geoeffective storms (Horne, Thorne, Glauert, et al., 2005; Thorne et al., 2013; Tu et al., 2014). In contrast, storm time chorus at mid to high latitudes causes microburst precipitation and may lead to losses of radiation belt electrons on the time scale of the order of a day (Lorentzen et al., 2001; Miyoshi et al., 2015; Thorne et al., 2005).

State of the art models of the Earth's radiation belts include the effects of wave-particle interactions as a diffusion process, but uncertainties over the diffusion rates remain. Diffusion rates have traditionally been computed using geomagnetic activity dependent global models of the average wave spectra and average ratio of the plasma frequency to the electron cyclotron frequency, f_{pe}/f_{ce} (Horne et al., 2013). Agapitov et al. (2019) demonstrated the importance of capturing the variability of f_{pe}/f_{ce} in the chorus-driven acceleration of electrons to relativistic energies. Specifically, the authors showed the reduction of f_{pe}/f_{ce} in association with increasing values of the AE index on the nightside of the Earth, combined with the decrease in the frequency of the peak wave amplitude with magnetic latitude, resulted in an order of magnitude change in the bounce averaged MeV electron diffusion rates when calculated using the local values of f_{pe}/f_{ce} and the mean wave spectra. More recently, the rare occurrences of ultrarelativistic (>7 MeV) electrons have been associated with depletions of plasma density to values $\sim 10\ \mathrm{cm}^{-3}$, and shown to be achievable through local acceleration by chorus waves when low plasma density conditions are considered (Allison et al., 2021).

The importance of using co-located measurements of the wave spectra and plasma properties in radiation belt modeling has recently been shown for plasmaspheric hiss (Agapitov et al., 2020; Watt et al., 2019) and electromagnetic ion cyclotron waves (Ross et al., 2020). Watt et al. (2019) showed that the mean pitch angle diffusion coefficients, $D_{\alpha\alpha}$, for plasmaspheric hiss, calculated by computing the average of $D_{\alpha\alpha}$ determined independently from the co-located measurements of the wave intensity and f_{pe}/f_{ce} were larger than those determined directly from the average values of the wave intensity and f_{pe}/f_{ce}. Agapitov et al. (2020) used simultaneous Van Allen probe measurements of the plasmaspheric hiss wave spectra and f_{pe}/f_{ce}, together with analytical estimates of the electron pitch angle diffusion coefficients, to compute bounce averaged electron pitch angle diffusion coefficients for relativistic electrons. Averaging these diffusion coefficients, Agapitov et al. (2020) found a 1.5–2 times decrease of MeV electron lifetimes for AE > 800 nT compared with using the Ozhogin et al. (2012) density model.

Similarly, Ross et al. (2020) showed that diffusion coefficients for electromagnetic ion cyclotron waves calculated by combining the effects of individual wave spectra and plasma properties resulted in diffusion over a wider range of energies and pitch angles. This significantly improved the agreement between the calculated decay of relativistic electrons and Van Allen Probe data when compared against existing diffusion models based on average wave spectra and plasma properties. In particular, the modeled fluxes during periods of decay were well captured, having been typically overestimated by a factor of 10 by the original method. These results mandate the development of new diffusion coefficients taking into account the co-located measurements of the wave spectra and f_{pe}/f_{ce}.

The wave normal angle (WNA) of chorus is also an important parameter in the computation of diffusion coefficients (Shprits & Ni, 2009) and is often modeled by a Gaussian distribution in $\tan(\psi)$, where ψ is the WNA (Albert, 2005; Glauert & Horne, 2005). Chorus waves are predominantly field aligned, but large WNAs have also been observed (Cattell et al., 2008; Hayakawa et al., 1984; Santolík et al., 2009). Recent statistical studies on the distributions of chorus WNAs show they are dependent on spatial location and geomagnetic activity (Agapitov et al., 2013, 2018; Li et al., 2013, 2016; Mourenas et al., 2014), as well as f_{pe}/f_{ce} (Taubenschuss et al., 2014) and distance from plasmaspheric plumes (Hartley et al., 2022). The inclusion of large WNAs in the computation of chorus pitch angle diffusion coefficients can result in increased pitch angle scattering, arising from the contribution of higher-order cyclotron resonances, and decreases in electron lifetimes (Artemyev et al., 2012; Mourenas

et al., 2012). It is therefore important to capture the variation in chorus WNAs, in a similar manner to local plasma conditions, in the computation of chorus diffusion rates.

In this study we use co-located near-equatorial wave and plasma properties from RBSP-A together with wave properties from the VLF database in Meredith et al. (2020) to compute new chorus diffusion coefficients, taking into account the effects of field aligned and oblique chorus waves. The new wave and plasma parameters are computed using the TS04 magnetic field model (Tsyganenko & Sitnov, 2005), to better capture the variability during active times. The paper is structured as follows. The methods used to combine the wave intensities from RBSP-A and the VLF database are described in Section 2 and the parameterization of the WNA is described in Section 3. The new diffusion coefficients are then presented in Section 4. The results are discussed and the conclusions presented in Sections 5 and 6, respectively.

2. Instrumentation and Data Analysis

In this section we use the average chorus wave intensity in the Meredith et al. (2020) VLF database, which covers absolute magnetic latitudes from the equator to 60°, to derive profiles for how chorus magnetic field intensity varies with absolute magnetic latitude. These profiles are used to map Van Allen Probes RBSP-A chorus wave intensity measurements to obtain co-located wave intensity and f_{pe}/f_{ce} measurements at higher latitudes.

2.1. Van Allen Probes

The Van Allen probes were launched on 30 August 2012 into highly elliptical orbits with a perigee of ∼1.1 R_E, an apogee of ∼5.8 R_E, and an inclination of 10° (Mauk et al., 2013). The satellites each had an orbital period of ∼9 hr and swept through the inner magnetosphere approximately five times per day, enabling them to study chorus waves from the plasmapause out to the spacecraft apogee.

For this investigation, we use approximately 7 years of plasma wave data from the Electric and Magnetic Field Instrument Suite and Integrated Science (EMFISIS) instrument (Kletzing et al., 2013) on board the Van Allen Probe A satellite from the time of the complete deployment of the electric field booms on the 7 November 2012 to the mission end on 14 October 2019. The magnetic field spectral densities and polarisation properties of the chorus waves were provided by the waveform receiver (WFR). This instrument measured the wave electric and magnetic fields in the frequency range from 2.1 Hz to 11.2 kHz and also provided the polarization properties, determined using the singular value decomposition method (Santolik et al., 2003). The electron plasma frequency, f_{pe}, was determined from measurements of the wave electric field by the high frequency receiver (HFR) (Kurth et al., 2015) and provided as a Level 4 data product. This instrument measured the wave electric field spectral density in the frequency range 10 kHz–487 kHz. The electron gyrofrequency was determined directly from the 1s measurements of the local magnetic field by the fluxgate magnetometer.

We first excluded data collected during thruster firings, periods of eclipse, and charging events. We also excluded intervals when the fluxgate magnetometer data were flagged as invalid, in calibration mode or in magFill mode. We then removed the instrumental background noise from the HFR electric field spectral density and the WFR magnetic field spectral density data using the technique described in Malaspina et al. (2017) and adopted in Wong et al. (2022). For the computation of L^* we use the TS04 external magnetic field model (Tsyganenko & Sitnov, 2005) and the International Geomagnetic Reference Field. To calculate the effects of chorus on the radiation belt electrons it is important to assess the waves along the drift path of the particle. Particles with different drift pitch angles have different drift paths and we use a pitch angle of 90° as an approximation when calculating L^*.

Chorus waves can overlap in frequency with plasmaspheric emissions such as plasmaspheric hiss and lightning generated whistlers (Meredith et al., 2012). These wave emissions cannot, therefore, be clearly identified based on frequency alone. However, chorus waves are largely observed outside the plasmapause (Meredith et al., 2001; Tsurutani & Smith, 1977). In contrast, plasmaspheric hiss and lightning generated whistlers tend to be observed in the plasmasphere (Platino et al., 2005; Thorne et al., 1973) and for the former, also plasmaspheric plumes (Summers et al., 2008). Electrostatic electron cyclotron harmonic (ECH) waves, which occur in bands between the harmonics of the electron gyrofrequency (Kennel et al., 1970), also tend to be restricted to the region outside of the plasmapause (Meredith et al., 2004) and plasmaspheric plumes. Consequently, we use the presence or

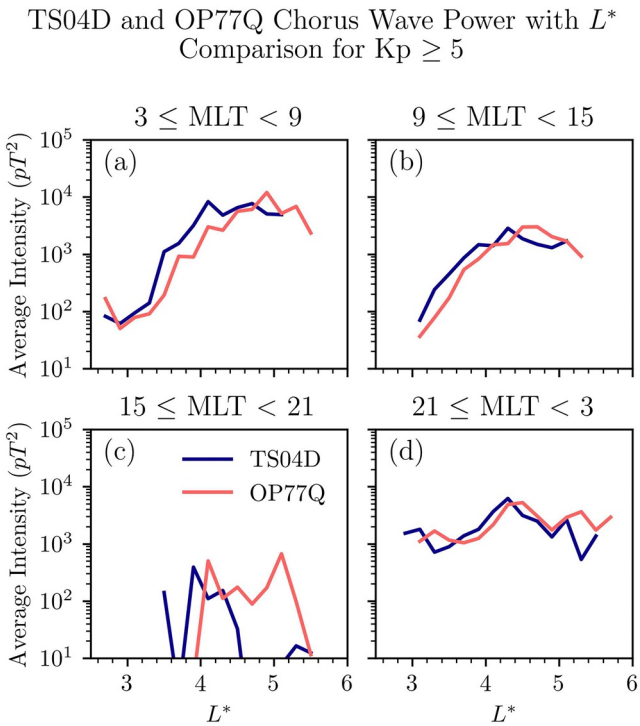

Figure 1. Comparison of the variation of chorus magnetic field intensity with L^* for TS04 (purple) and Olson-Pfitzer (pink) in four MLT sectors with Kp ≥ 5. We include all magnetic latitudes sampled by Van Allen Probe A, requiring a minimum of 200 samples in each L^*, MLT bin for $\lambda < 10°$ to ensure sufficient equatorial coverage, and exclude L^*, MLT bins with less than 600 samples.

absence of ECH waves to determine whether the satellite is outside or inside the plasmapause, respectively. Specifically, for $L^* \geq 2.5$, if the measured ECH wave intensity is non-zero then the spacecraft is identified as outside the plasmapause. Measurements inside of $L^* = 2.5$ are considered inside the plasmapause. In order to remove contributions from spikes in the HFR data and gaps in the ECH wave intensity, which result in short duration changes in the plasmapause identification, we remove identification changes lasting less than 500 s in duration by assuming the same environment as either side of the identification change. It is also possible for the third harmonic band to fall below the lower frequency limit of the HFR instrument, and when the upper limit of the third harmonic band, $4f_{ce}$, falls below the lower limit of the HFR instrument the ECH wave intensity can not be determined. In such cases, we use the criteria based on plasma density in Li et al. (2015), and ignore times when neither criteria is applicable.

Non-zero magnetic field spectral density measurements outside the plasmapause with frequency in the range $f_{LHR} < f < f_{ce}$ are identified as chorus, where f_{LHR} and f_{ce} are the local lower hybrid resonance frequency and the local electron gyrofrequency, respectively. We compute the chorus wave intensity in $0.1f_{ce}$ frequency bands with the lowest frequency band spanning the range $f_{LHR} < f < 0.1f_{ce}$, and separate lower and upper band chorus at $0.5f_{ce}$. We also work with the equatorial values f_{pe}/f_{ce}^{eq} obtained by mapping local f_{pe}/f_{ce} measurements to the equator assuming constant plasma density and a dipole magnetic field. Figure 1 compares the variation of chorus wave intensity with L^* between the external magnetic field models TS04 and Olson-Pfitzer for four MLT sectors during active conditions Kp ≥ 5. The comparison is shown for active conditions where the difference between the models is likely to be largest since Olson-Pfitzer is a quiet time model while TS04 varies with solar wind parameters and components of the interplanetary magnetic field. In the morning sector, Figure 1a, we observe higher chorus wave intensity between $3 < L^* < 4.7$ for TS04. This trend is also present in the other three MLT sectors, with TS04 generally having larger chorus wave intensity at $L^* < 4$ but not extending out past $L^* = 5.5$. The mapping to magnetic coordinates results in coverage to a slightly higher L^* when using the Olson-Pfitzer quiet time model which explains why the wave intensity extends to slightly higher L^* values (pink lines) when using this model. The reason for the difference in the maximum extent in L^* is not immediately obvious. Although the RBSP orbit extends out to the same radial distance, the field is more distorted using TS04 and compressed on the dayside. In this case the electron drift paths extend to larger radial distance to conserve the first adiabatic invariant and, thus, a satellite on the dayside only samples lower L^*.

2.2. VLF Database

The Van Allen probes measure wave and plasma properties within 21° of the magnetic equator. However, chorus can extend to higher latitudes, primarily on the dayside (Agapitov et al., 2018; Li et al., 2009; Meredith et al., 2001; Miyoshi et al., 2013), where it can significantly affect radiation belt dynamics (Thorne et al., 2005; Wang & Shprits, 2019). To extend our analysis to higher latitudes we use the VLF database described in Meredith et al. (2020). This database contains wave data from eight satellites, including approximately 3 years of data from Dynamics Explorer 1 (DE1), 1 year of data from Double Star TC1, 10 years of data from Cluster 1, 8 years of data from each of Time History of Events and Macroscale Interactions during Substorms (THEMIS)-A, THEMIS-D, and THEMIS-E, and 3 years of data from the Van Allen probes RBSP-A and RBSP-B.

The database contains average chorus wave intensity for $1 < L^* < 10$ in 0.1 L^* bins, 1 hr MLT bins, 3° magnetic latitude bins for $-60° \leq \lambda < 60°$ and 10 unit sized bins in Kp. The British Antarctic Survey (BAS) Radiation Belt forecasting model uses the Kp index to drive the model, due to the availability of 24 hr forecasts of this index. Consequently, we use the Kp index in this study. The VLF database was created using the Olson-Pfitzer quiet time model (Olson & Pfitzer, 1977) and the International Geomagnetic Reference Field, assuming a pitch angle

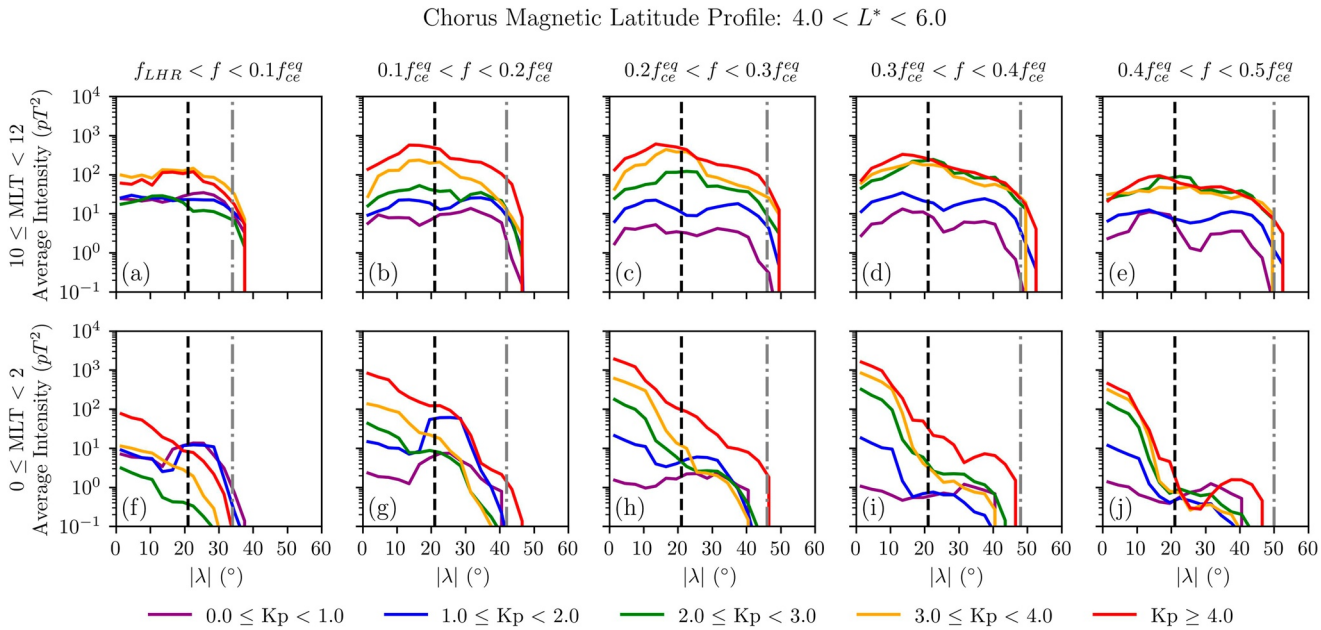

Figure 2. Average lower band chorus wave intensity as a function of absolute magnetic latitude, |λ|, in the regions $10 \leq$ MLT < 12 (top panels) and $0 \leq$ MLT < 2 (bottom panels) for, from left to right, increasing normalized frequency. Variation with geomagnetic activity, parametrized by Kp, is shown in colors varying from purple through to red. The vertical black dashed line shows the maximum magnetic latitude of the Van Allen probes and the gray dash-dotted line is the magnetic latitude above which $f_{LHR}^{D} > 0.1(i+1)f_{ce}^{eq}$ for frequency band i, where $i = 0, \ldots, 4$.

of 90° in the calculation of L^*. The magnetic latitude was calculated using a dipole magnetic field model. The plasmapause identification is satellite dependent due to the different instruments deployed in each mission and the parameters available at the time of the creation of the database. For THEMIS the criteria in Li et al. (2010), based on the plasma density, is used, while for DE1, Cluster 1, Double Star TC1, RBSP-A and RBSP-B the plasmapause is determined using the Carpenter and Anderson (1992) model, which is driven by the maximum value of Kp in the last 24 hr.

The chorus wave magnetic field intensity is binned in 10 frequency bands from the local lower hybrid resonance to the local electron gyrofrequency, where first frequency band extends from f_{LHR} to $0.1f_{ce}$, and the others have width $0.1f_{ce}$. The lower hydrid resonance is computed using the high density approximation due to density measurements being unavailable for some of the satellites in the database.

2.3. VLF Database Latitude Profile

To determine how the wave intensity of a chorus wave generated at a fixed equatorial frequency changes as the wave propagates along a magnetic field line to higher latitudes we first renormalize the wave intensity from frequency bands normalized to the local electron gyrofrequency to frequency bands normalized to the equatorial electron gyrofrequency. The method used to renormalize the frequency bands is described in Appendix A using the wave spectra in 3° absolute magnetic latitude bins from the equator to 60°, 2 hr MLT bins, $2L^*$ bins $2 \leq L^* < 4$ and $4 \leq L^* < 6$, and 5 Kp bins $0 \leq$ Kp < 1, $1 \leq$ Kp < 2, $2 \leq$ Kp < 3, $3 \leq$ Kp < 4, and Kp ≥ 4. With the wave intensity in equatorial electron gyrofrequency bands we compute a profile for how the wave intensity in each frequency band varies with absolute latitude from the equator to 60° magnetic latitude, ignoring bins with less than 50 data counts. To smooth the variation of wave intensity with latitude a rolling average with adjacent latitude bins is performed. Any chorus wave intensity in the bins with $L^* < 4$ and Kp < 2 is ignored as the data has poor coverage of the full magnetic latitude range.

Figure 2 shows the average wave intensity of lower band chorus as a function of magnetic latitude in five normalized frequency bands, with normalized frequency increasing from left to right, and two MLT sectors, one on the dayside, $10 \leq$ MLT < 12 (top panels) and one on the nightside $0 \leq$ MLT < 2 (bottom panels). Variation with geomagnetic activity, as monitored by Kp, is shown by different colors. In agreement with previous statistical

studies, the profiles on the nightside have peak wave intensity near the equator and decreases rapidly with latitude. In contrast to this, the dayside chorus wave intensity peaks at intermediate latitudes and exhibits a much flatter profile with latitude. The vertical black dashed line shows the maximum magnetic latitude of the Van Allen probes and the gray dash-dotted line is the magnetic latitude Λ_i above which the lower hybrid resonance frequency, computed using $L = 5$ and magnetic latitude Λ_i in a dipole field, f^D_{LHR}, satisfies

$$f^D_{LHR} > 0.1(i+1)f^{eq}_{ce}, \tag{1}$$

for frequency band i, where $i = 0, \ldots, 4$. As the local lower hybrid resonance frequency is greater than the upper limit of band i at $\lambda > \Lambda_i$ the wave intensity in this band is not captured by the VLF database at these latitudes.

2.4. Mapping Van Allen Probe Measurements to Different Latitudes

The VLF database latitude profile in combination with the local Van Allen probes measurements allow us to estimate measurements of chorus wave intensity from the magnetic equator to a maximum magnetic latitude of 60°. The upper limit of the latitudinal extent is a function of normalized frequency, as can be seen in Figure 2, and the latitudinal extent ranges from 40° in the lowest frequency band to 55° in the highest frequency band. The Van Allen Probe wave spectra observations are first mapped from frequency bands normalized to the local electron gyrofrequency to bands normalized to the equatorial electron gyrofrequency assuming a dipole field. Each wave magnetic field intensity measurement is then mapped to a designated latitude $\hat{\lambda}$ as follows:

1. The L^*, MLT and Kp value of the observation selects out a unique profile with latitude for each frequency band, $\mathcal{B}_i(\lambda)$, derived from the VLF database
2. The wave intensity of frequency band i at the designated latitude, $\hat{B}_i$, is given by

$$\hat{B}_i = \frac{\mathcal{B}_i(\hat{\lambda})}{\mathcal{B}_i(\lambda_{obs})} B_{i,obs}, \tag{2}$$

where λ_{obs} and $B_{i,obs}$ is the magnetic latitude and wave intensity in frequency band i, respectively, of the observation. This mapping ensures that $\hat{B}_i = B_{i,obs}$ when $\hat{\lambda} = \lambda_{obs}$. As previously mentioned, the magnetic latitude profiles derived using the VLF database uses L^* computed with the Olson and Pfitzer (1977) magnetic field model while the Van Allen probes data uses TS04 (Tsyganenko & Sitnov, 2005). We minimize the effects of using different magnetic field models by using large L^* bins in the derivation of the magnetic latitude profiles.

The mapping of Van Allen Probe chorus wave spectra observations from local electron gyrofrequency bands to equatorial electron gyrofrequency bands using a dipole field is only valid when the ratio $(B/B_{eq})^{TS04}$, where B and B_{eq} are the local and equatorial external magnetic field magnitude, respectively, is similar to the dipole equivalent, $(B/B_{eq})^D$, at the latitude of the observation. When $(B/B_{eq})^{TS04} > (B/B_{eq})^D$, the equatorial wave spectrum obtained from binning the chorus wave magnetic field intensity in terms of the TS04 equatorial electron gyrofrequency, computed using the minimum magnetic field magnitude of the field line of the measurement in the TS04 magnetic field model, peaks at a higher relative frequency compared with using a dipole field. The two equatorial wave spectra can therefore be very different if the difference between $(B/B_{eq})^{TS04}$ and $(B/B_{eq})^D$ is large, in which case the equatorial wave spectra derived using the dipole field is no longer a reasonable approximation.

The differences in the ratio B/B_{eq} between TS04 and the dipole field can be phrased in terms of the difference between the magnetic latitude of the observation, λ, and the magnetic latitude, λ^D, required for the dipole field to satisfy

$$(B/B_{eq})^D = (B/B_{eq})^{TS04}. \tag{3}$$

Figure 3 shows the average absolute difference $|\lambda - \lambda^D|$ as a function of L^* and MLT for different levels of geomagnetic activity, measured by Kp. The largest differences in the two magnetic latitudes occur for $L^* \geq 4$ on the nightside between $18 \leq \text{MLT} < 5$. In this region the intensity of the chorus emissions peak near the equator and decrease rapidly with increasing magnetic latitude (Figure 2, bottom panels). Here we use the local observations of the wave intensity and f_{pe}/f^{eq}_{ce}. Elsewhere, we map the observations along the field line using the magnetic latitude profile.

A comparison of the latitude dependence of the average lower and upper band chorus wave intensities from the Van Allen probes measurements and the same measurements mapped to latitudes between the magnetic equator and 60° magnetic latitude using the VLF database profiles is shown in Figure 4. Average intensities are shown

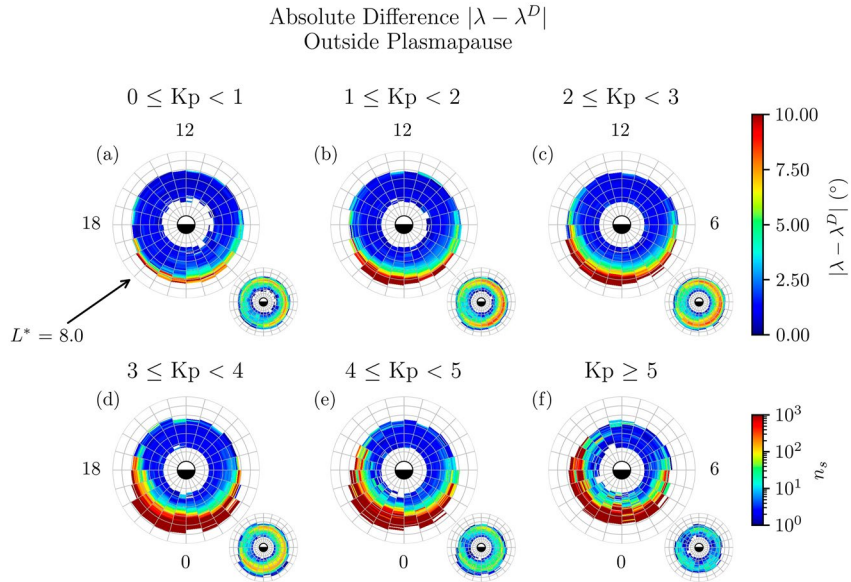

Figure 3. Global maps of the absolute difference between the magnetic latitude λ and λ^D, the magnetic latitude at which $\left(B/B_{eq}\right)^D = \left(B/B_{eq}\right)^{TS04}$, as a function of L^* and MLT for six different geomagnetic activity levels, as monitored by Kp. The maps extend linearly out to $L^* = 8.0$ with noon at the top and dawn to the right. The average differences are shown in the large panels and the corresponding sampling distributions are shown in the small panels.

for the dayside $6 \le$ MLT < 15, for active conditions, Kp ≥ 4. For lower band chorus, the mapped intensities, Figure 4b, have larger wave intensity in the near equatorial region for $L^* > 4$ than that observed in the Van Allen probes data Figure 4a. This suggests that the gradient in the Van Allen Probe wave intensity with magnetic latitude is steeper than that derived from the VLF database in this region. This can also be seen in the gradual change in the chorus wave intensity with latitude in the mapped intensities for $L^* > 4$ compared with the Van Allen probes data, which, for some L^*, exhibits an order of magnitude change in wave intensity from the equatorial region to

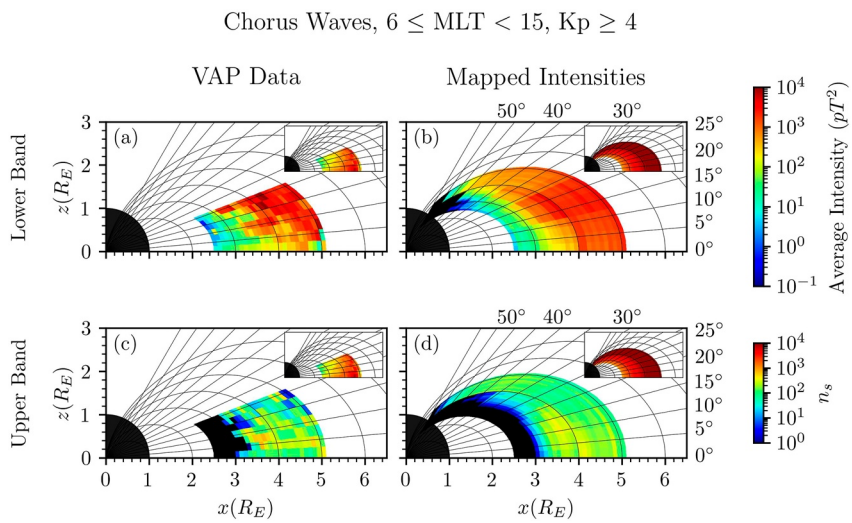

Figure 4. Global maps of the average wave intensity of lower and upper band chorus waves in the meridional plane during active conditions, Kp ≥ 4, for $6 \le$ MLT < 15. Panels (a) and (c) show average intensities from Van Allen Probe measurements, while (b) and (d) show the average intensities obtained from mapping the Van Allen Probe measurements to latitudes between $0° \le |\lambda| \le 60°$ using the VLF database derived latitude profile. We have included dipole field lines and lines of constant magnetic latitude to aid visualization of the data. The average wave intensities are displayed in the large panels and the associated sampling distributions in the small panels. Measurements with $L^* > 5.5$ are omitted due to the lack of full MLT coverage.

15°. In particular for both lower and upper band chorus at $L^* > 4$, the increase in average intensities observed by the Van Allen Probes between the equator and 5° is not reproduced by the mapped intensities. However, the variation of the chorus wave intensity in the near-equatorial region is more consistent with the results presented in Figure 4 of Meredith et al. (2020). At $L^* < 4$, the increase in lower band chorus wave intensity with increasing magnetic latitude up to $\lambda < 20°$ in the mapped intensities are consistent with the Van Allen Probe observations. Strong lower band chorus wave intensity is observed to extend higher latitudes in the region $6 \leq \text{MLT} < 15$, consistent with observations (Meredith et al., 2014). The mapped intensities for upper band chorus are generally consistent with that observed in the Van Allen probes data, though the peak in the upper band chorus wave intensity at $L^* = 3.5$ between $5° \leq \lambda < 10°$ is not quite captured, due to the smoother magnetic latitude profiles used in deriving the mapped intensities.

3. Chorus Wave Normal Angle

The computation of diffusion coefficients requires a parametrization of the wave power distribution as a function of WNA (Glauert & Horne, 2005; Lyons, 1974), which enters into the dispersion relation and resonance condition, and can significantly impact the resulting diffusion rates (Agapitov et al., 2018; Artemyev et al., 2012; Mourenas et al., 2012; Shprits & Ni, 2009). In this section we study the probability density functions of the WNA of lower and upper band chorus and their dependence on spatial location and local plasma conditions, described by f_{pe}/f_{ce}^{eq}. This method captures the occurrences of both high and low power waves and we subsequently fit the probability density functions as an approximation to the wave power distributions as a function of WNA.

3.1. Distribution Fits

The WNAs were determined from individual WNA values as determined by the single value decomposition method applied to narrow frequency ranges (Santolik et al., 2003). Since the WNA varies with normalized frequency (Li et al., 2016) we determined WNAs for upper and lower band chorus separately, weighting the individual measurements by the magnetic intensity to give greater weighting to the stronger waves. We use the equatorial electron gyrofrequency, computed using the minimum magnetic field magnitude of the field line of the measurement using the TS04 magnetic field model, to determine the frequency bands for lower and upper band chorus. The equatorial values f_{pe}/f_{ce}^{eq} are computed by mapping the local values down to the equator assuming constant plasma density and a dipole field. The distributions depend on magnetic latitude and MLT, which we initially split into 6° and 1 hour bins, respectively. Figure 5 shows the probability density function of the WNA for lower band chorus in the region $0° \leq |\lambda| < 6°$. Between $8 \leq \text{MLT} < 21$ the WNA distributions are well approximated by a single Gaussian distribution (orange dashed curves), with peak $\psi_m \sim 11°–13°$. Wave normal angle distributions exhibiting two peaks with a minimum around 40° are found between $21 \leq \text{MLT} < 8$. The occurrence of a population of chorus waves with large WNA on the nightside through to dawn at low latitudes agrees with the recent results in Agapitov et al. (2018). Similar double peaked distributions of lower band WNA have been observed in Hartley et al. (2022) near the presence of plasmaspheric plumes. However, as plasmaspheric plumes are usually found between $15 \leq \text{MLT} < 23$, the large WNA chorus found in the distributions studied here are likely to be a different population. As only the magnetic field intensity is considered in the computation of the intensity weighted WNA, the total wave intensity of oblique waves is underestimated and if the total magnetic and electric field intensity were considered the occurrence of the large intensity weighted WNAs is likely higher than in the results shown here.

For the other MLT bins, which have two distinct peaks in the WNA distribution we explore the dependency on L^*, f_{pe}/f_{ce}^{eq} and Kp to determine whether the small and large WNA distributions can be separated. In order to preserve a statistically significant number of samples in each spatial bin, we combine the data in the MLT bins exhibiting distributions with two peaks to allow further binning of the data by other dependencies. The WNA distributions show little dependence on Kp but exhibit a distinctive trend dependent on L^* and f_{pe}/f_{ce}^{eq}. This is shown in Figure 6, for $0° \leq |\lambda| < 6°$ and $21 \leq \text{MLT} < 8$. Distributions well approximated by a single Gaussian are plotted as in Figure 5 while for those with two distinctive peaks we find the value of the WNA, ψ_{sep}, at the local minimum between the two peaks and fit the two peaks either side of this value with two separate Gaussian distributions, a small WNA distribution (orange dashed line) and a large WNA distribution (pink dashed line).

From the figure we can see that the large WNA distribution is more dominant at high L^* and low f_{pe}/f_{ce}^{eq}. In the lowest L^* bin the WNA distribution is modeled well with a single Gaussian fit at small WNA values. As

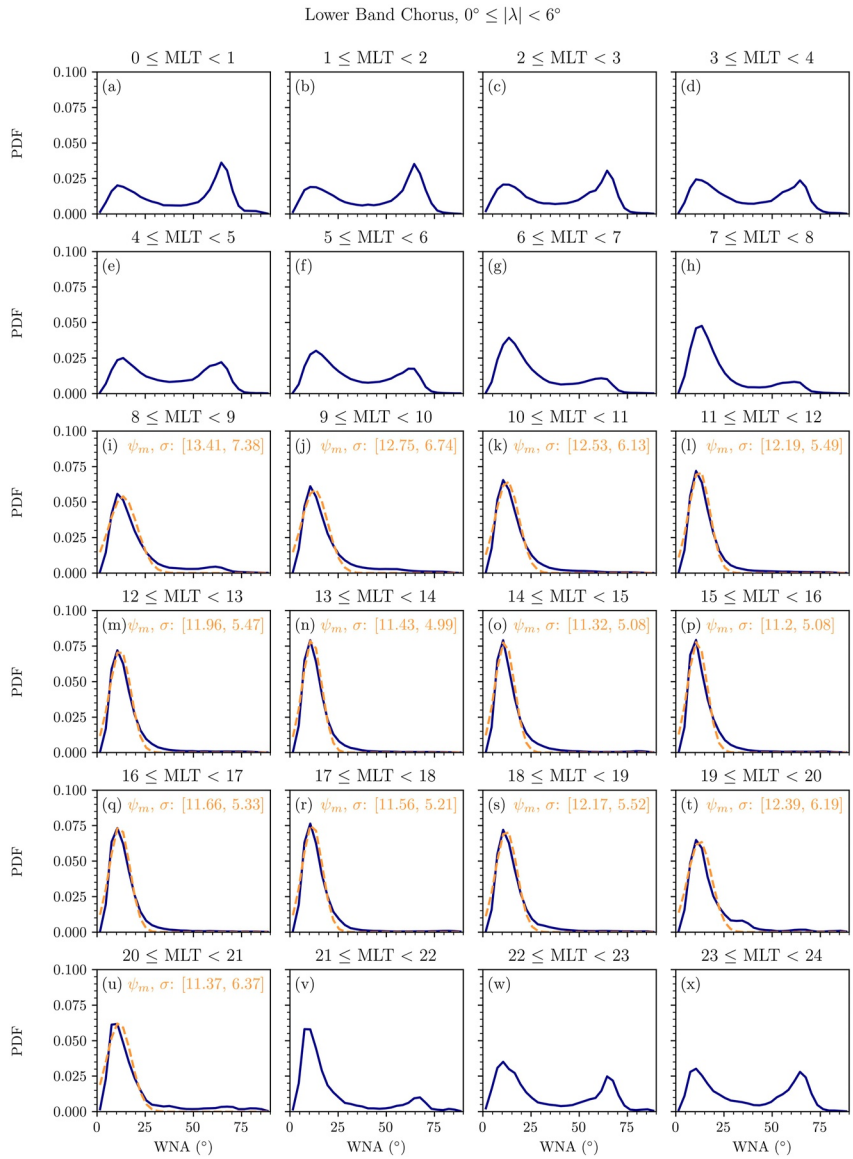

Figure 5. Probability density function of the wave normal angle of lower band chorus in magnetic latitude bin $0° \leq |\lambda| < 6°$ for each 1 hr sector in MLT (purple solid lines). For the distributions which can be well approximated by a single Gaussian, the orange dashed curves plot the Gaussian fit, $g(\psi)$, with the mean, ψ_m, and standard variation, σ, given in each plot.

L^* increases we observe a large WNA distribution emerging at the low f_{pe}/f_{ce}^{eq} bins and at $5.25 \leq L^* < 6.25$, the distribution is dominated by large WNAs in the lowest f_{pe}/f_{ce}^{eq} bin with the large WNA Gaussian peaking at $\psi_m = 65.31°$. Increasing f_{pe}/f_{ce}^{eq} at this largest L^* bin decreases the occurrence of the large WNAs until we are left with a single Gaussian distribution peaked at $\psi_m = 11.93°$ in the highest f_{pe}/f_{ce}^{eq} bin. Higher occurrence of chorus with large WNA when f_{pe}/f_{ce}^{eq} is low and smaller WNAs at large f_{pe}/f_{ce}^{eq} was also observed in Taubenschuss et al. (2014) using data from THEMIS. At higher latitudes the peak WNA and variance for the small and large WNA distributions is larger, consistent with previous observations (Agapitov et al., 2013; Mourenas et al., 2014) and ray tracing results (Breuillard et al., 2012; Chen et al., 2013). A similar trend in the variation of the WNA distribution with increasing L^* and f_{pe}/f_{ce}^{eq} is seen for $6° \leq |\lambda| < 12°$, while for $|\lambda| \geq 12°$ double peaked distributions with a small and large WNA distribution occur for $f_{pe}/f_{ce}^{eq} < 16.2$ but do not show strong trends with L^* and f_{pe}/f_{ce}^{eq}, as seen at lower latitudes. The occurrence of the second peak at large WNAs reduces to a much smaller MLT sector $7 \leq \text{MLT} < 11$ for $|\lambda| \geq 18°$, agreeing with the observations in Haque et al. (2010) using data from the Polar spacecraft that chorus with large WNA has a lower occurrence at higher latitudes. However, increased occurrence and higher wave intensity for oblique chorus waves at higher latitudes

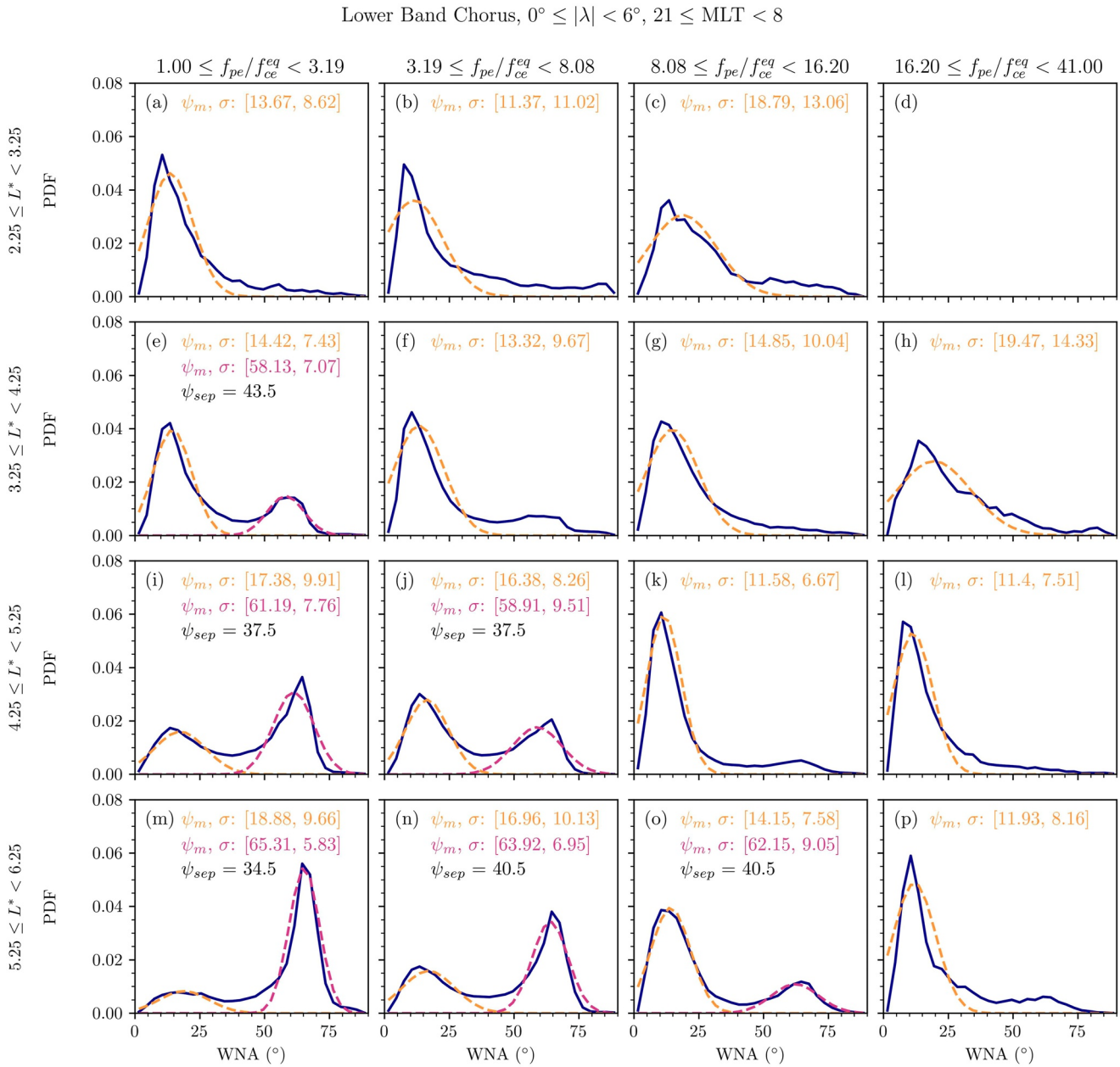

Figure 6. Probability density function of the wave normal angle of lower band chorus in the region $0° \leq |\lambda| < 6°$ for $21 \leq \text{MLT} < 8$ (purple solid lines). The results are shown for, from top to bottom, increasing L^* and from left to right, increasing f_{pe}/f_{ce}^{eq}. For the distributions which can be well approximated by a single Gaussian, the orange dashed curves plot the Gaussian fit with the mean, ψ_m, and standard variation, σ, given in each plot. For those with two distinctive peaks we fit the two peaks either side of ψ_{sep} with two separate Gaussian distributions, a small wave normal angle (WNA) distribution (orange dashed line) and a large WNA distribution (pink dashed line).

has been observed in data from the Cluster mission (Mourenas et al., 2014). It was shown in Li et al. (2016) that the occurrence of large WNAs in lower band chorus is dependent on frequency, with higher occurrences arising close to the resonance cone angle for frequencies above $0.15f_{ce}$. This frequency dependence is not captured in this analysis, which studies the wave intensity weighted average of the WNA in lower and upper band chorus. A summary of the parameters of the Gaussian fits for lower band chorus WNA distributions is given in Tables B1–B3 in Appendix B.

For upper band chorus, the distributions often do not take the form of a single Gaussian distribution, or two separate Gaussian distributions, and the lower number of data points means larger spatial bins are required to

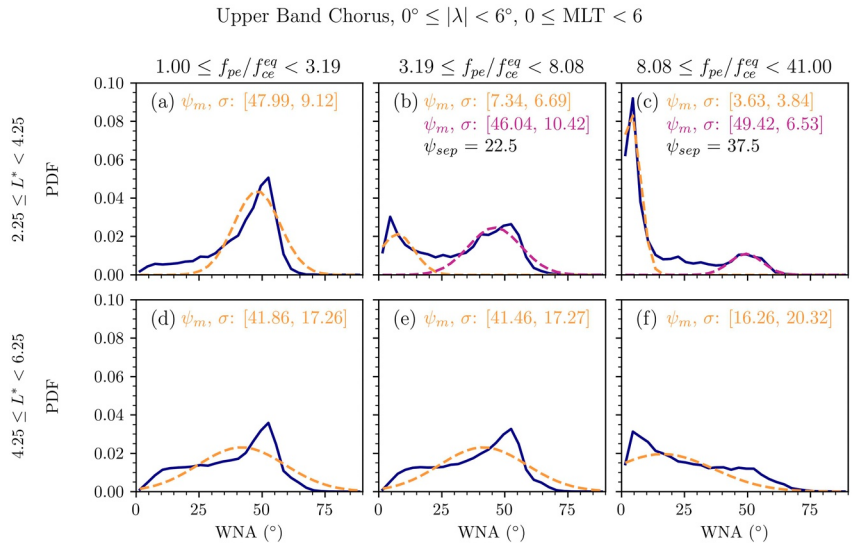

Figure 7. Probability density function of the wave normal angle of upper band chorus in the region $0° \le |\lambda| < 6°$ for $0 \le \text{MLT} < 6$ (purple solid lines). The results are shown for $2.25 \le L^* < 4.25$ (top panels) and $4.25 \le L^* < 6.25$ (bottom panels) and, from left to right, increasing f_{pe}/f_{ce}^{eq}. For the distributions which can be well approximated by a single Gaussian, the orange dashed curves plot the Gaussian fit with the mean, ψ_m, and standard variation, σ, given in each plot. For those with two distinctive peaks we fit the two peaks either side of ψ_{sep} with two separate Gaussian distributions, a small wave normal angle (WNA) distribution (orange dashed line) and a large WNA distribution (pink dashed line).

separate the data by L^*, MLT, λ and f_{pe}/f_{ce}^{eq}. We fit the WNA distribution in two L^* bins for $2.25 \le L^* < 4.25$, $4.25 \le L^* < 6.25$, 6 hr MLT bins, 6° magnetic latitude bins and 3 logarithmic bins in f_{pe}/f_{ce}^{eq}, $1 \le f_{pe}/f_{ce}^{eq} < 3.19$, $3.19 \le f_{pe}/f_{ce}^{eq} < 8.08$, $8.08 \le f_{pe}/f_{ce}^{eq} < 41$. For the distributions with two distinct peaks and a local minimum in between, located at ψ_{sep}, we fit the two peaks either side of the local minimum with a single Gaussian distribution where the orange and pink dashed lines show the fits for the small and large WNA distributions, respectively. For the other distributions, we fit a single Gaussian distribution. Figure 7 shows the upper band chorus WNA distributions for $0° \le |\lambda| < 6°$ and $0 \le \text{MLT} < 6$ bin. The parameters for the WNA distributions for upper band chorus are given in Appendix B Tables B4–B7.

3.2. Separating Chorus With Small and Large WNA

From the analysis of lower and upper band chorus WNAs, the population of chorus with large WNA can be significant in conditions with low f_{pe}/f_{ce}^{eq}. Using the VLF database derived latitude profile to map chorus wave intensities to higher latitudes assumes the waves propagate along the field line. In order to capture the effect of the chorus with large WNA observed in the Van Allen probes data we separate the wave intensities into those associated with small and large WNA using the WNA distributions in Tables B1–B7.

We first assign each Gaussian distribution in Tables B1–B7 to either be a small or large WNA distribution. For the WNA distributions with two peaks this is done automatically, where the distribution with mean $\psi_m < \psi_{sep}$ is identified as a small WNA distribution. For the bins with only a single Gaussian distribution $g(\psi)$ with mean ψ_m, the identification is carried out using the following criteria

$$\text{Lower Band:} \quad g(\psi) = \begin{cases} \text{Small WNA} & \text{if } \psi_m < 42° \\ \text{Large WNA} & \text{otherwise} \end{cases}$$

$$\text{Upper Band:} \quad g(\psi) = \begin{cases} \text{Small WNA} & \text{if } \psi_m < 36° \\ \text{Large WNA} & \text{otherwise} \end{cases} \qquad (4)$$

where the values of 42° and 36°, which are close to the mean of the ψ_{sep} values across all bins, were chosen taking into account the mean of ψ_{sep} and then visually inspecting its compatibility with the peaks of the single Gaussian

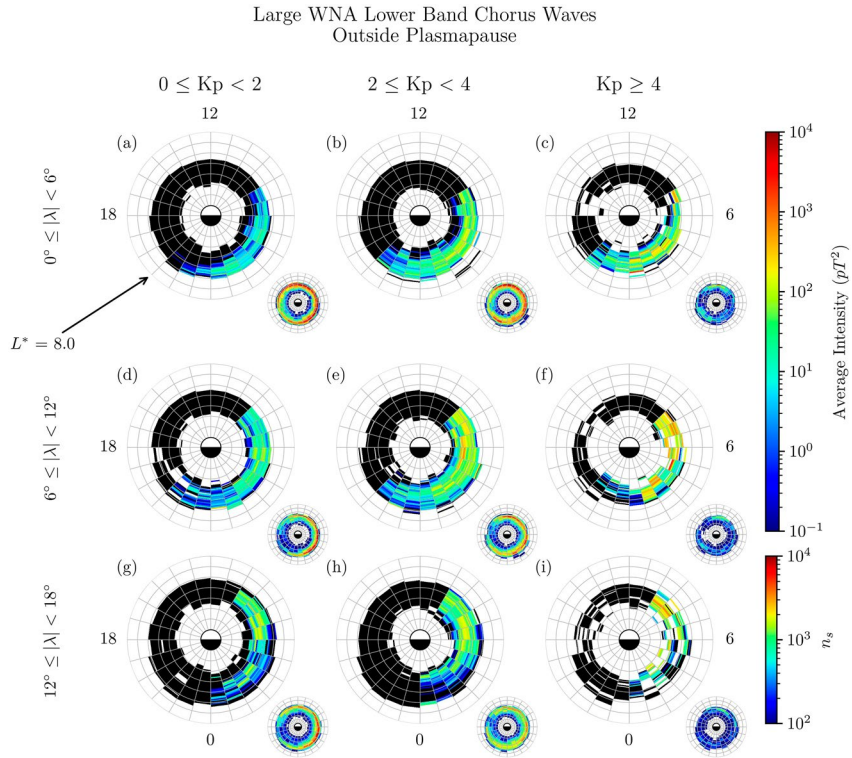

Figure 8. Global maps of the average wave intensity of lower band chorus with large wave normal angle as a function of L^* and MLT for increasing absolute magnetic latitude, top to bottom, and increasing geomagnetic activity, left to right, as monitored by Kp. The maps extend linearly out to $L^* = 8.0$ with noon at the top and dawn to the right. The average wave intensities are displayed in the large panels and the associated sampling distributions in the small panels.

distributions. The distributions identified as a large WNA distribution under this criteria are highlighted in bold in Tables B1–B7.

For a lower band chorus measurement with wave intensity weighted WNA $\hat{\psi}$ we determine the WNA distribution, Ψ_{LB}, for the spatial location and f_{pe}/f_{ce}^{eq} bin of the measurement using Tables B1–B7. If Ψ_{LB} is fitted with a single Gaussian distribution $g(\psi)$ then the measurement is classified in the same way $g(\psi)$. If Ψ_{LB} consists of two Gaussian distributions then the measurement is considered part of the small WNA distribution if $\hat{\psi} < \psi_{sep}$ and a measurement of the large WNA distribution otherwise. Figure 8 shows global maps of the average wave intensity of the large WNA lower band chorus as a function of L^* and MLT for, from top to bottom, increasing magnetic latitude and from left to right increasing geomagnetic activity. In the near equatorial region, $|\lambda| < 6°$ (top panels), peak average intensities are around 100 pT^2 and occur in the dawn sector between 0 and 8 MLT. The trend of the large WNA chorus coming into lower L^* with increasing activity is in agreement with Li et al. (2016). It is interesting to note that the region of chorus with large WNAs is restricted in MLT and is not observed at noon or in the afternoon sector. We note that there are regions on the dayside where there is very little wave intensity at low latitudes but significant wave intensity at higher latitudes, for example, around 9 MLT. This suggests that the waves maybe generated at higher latitude or propagate into that region from other locations. Diffusion due to that latitudinal distribution of these waves is taken into account in the results below.

Figure 9 shows global maps of the average wave intensity of the small WNA lower band chorus in the same format as Figure 8. Here large intensities are seen during active conditions (right hand panels) from 22 MLT through dawn to 14 MLT. All of the wave intensity near noon and in the afternoon sector is associated with small WNAs, as wave intensity in this region is completely absent at large WNAs.

4. Chorus Diffusion Coefficients

Having separated the wave intensities into those associated with small and large WNA, we compute bounce and drift averaged diffusion coefficients as functions of pitch angle and energy for chorus with small and large WNA

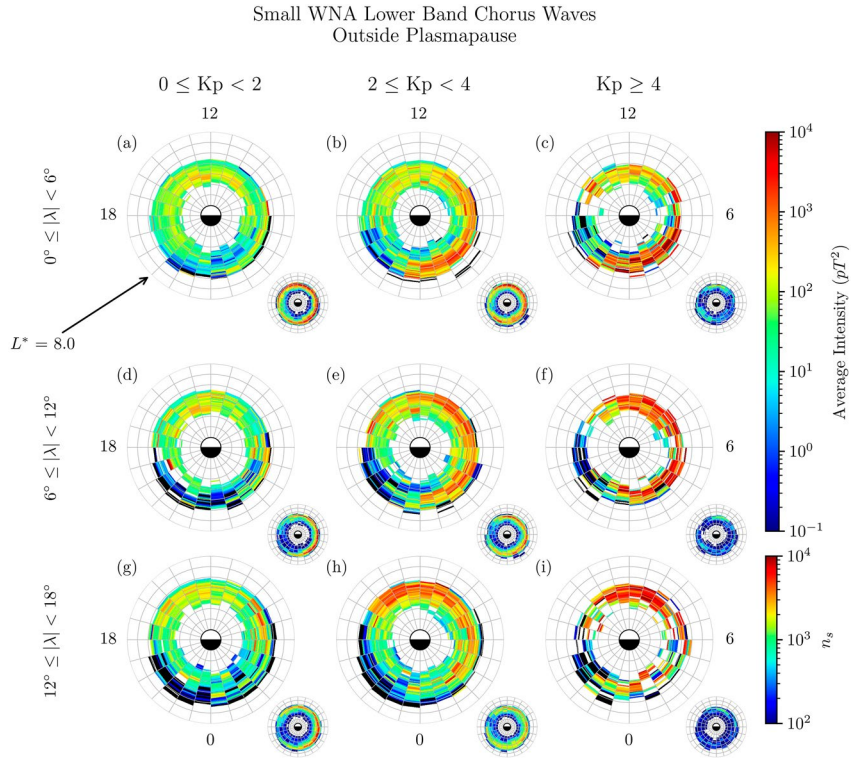

Figure 9. Global maps of the average wave intensity of lower band chorus with small wave normal angle as a function of L^* and MLT for increasing absolute magnetic latitude, top to bottom, and increasing geomagnetic activity, left to right, as monitored by Kp. The maps extend linearly out to $L^* = 8.0$ with noon at the top and dawn to the right. The average intensities are shown in the large panels and the corresponding sampling distributions are shown in the small panels.

using the associated wave intensities and the probability density functions of the WNA described in Section 3. The resulting diffusion coefficients depend on L^* and geomagnetic activity, as recorded by Kp.

4.1. Computation Method

In this study we use the data-driven version of the PADIE code which uses averaged measured spectra as opposed to gaussian fits (Glauert & Horne, 2005; Ross et al., 2021). We incorporate the variability of f_{pe}/f_{ce}^{eq} by additionally binning the observations by f_{pe}/f_{ce}^{eq}, as in Ross et al. (2021). First, the chorus wave intensity in the 10 normalized frequency bands and the magnetic latitude of each Van Allen Probe observation is binned as a function of L^*, MLT, f_{pe}/f_{ce}^{eq} and Kp index. We adopt seven L^* bins in the range $2.25 \leq L^* \leq 5.75$ in steps of $0.5L^*$, 24 MLT bins in steps of 1 hr of MLT, and 16 logarithmically spaced bins of the ratio f_{pe}/f_{ce}^{eq}, from $1 \leq f_{pe}/f_{ce}^{eq} \leq 41$. The geomagnetic activity is divided into six bins as monitored by the Kp index as follows: $0 \leq \text{Kp} < 1$, $1 \leq \text{Kp} < 2$, $2 \leq \text{Kp} < 3$, $3 \leq \text{Kp} < 4$, $4 \leq \text{Kp} < 5$ and $\text{Kp} \geq 5$. The sizes of these bins were selected to capture the variability with activity whilst maintaining a sufficient number of samples for good statistics. We excluded bins with less than 100 samples from the computation of diffusion coefficients due to having poor statistics.

We compute separate diffusion coefficient matrices for small and large WNA chorus including resonances between -10, …, 10 and the Landau resonance $n = 0$. The determination of the wave spectra in each magnetic latitude bin depends on L^* and MLT and the full details on the computation of the diffusion coefficients can be found in Appendix C. While the WNA distributions are fitted with the Gaussian distribution in Equation B1, PADIE uses a WNA distribution described by a Gaussian in $X = \tan(\psi)$. Using the mean and standard deviation fitted in Section 3 to compute the Gaussian in X produces distributions which are narrower than the original fitted distributions, especially for large WNAs. It was shown in Kersten (2016) that a smaller width in the WNA distribution generally results in smaller diffusion coefficients, with the effect most prominent for upper band chorus. However, the effect of reducing the WNA distribution width from 30° to 15° for field aligned waves was found to have an insignificant effect on the pitch angle diffusion coefficients for energies greater than 10 keV.

Furthermore, it was also shown in Shprits and Ni (2009) that the diffusion coefficients of high energy electrons are relatively insensitive to the WNA distribution and we therefore do not expect the differences to significantly affect the resulting diffusion coefficients.

While we have separated each chorus measurement into either a small or large WNA measurement, the diffusion coefficients for each WNA distribution is still computed by averaging over all measurements outside the plasmapause, including times when no chorus waves are observed, or when the chorus wave observed is not of the required WNA distribution. More specifically, a chorus wave observation identified as having large WNA using the criteria in Section 3.2 is equivalent to an observation with no chorus wave intensity in the computation of the small WNA chorus diffusion coefficients, and vice versa. We subsequently calculate the bounce and drift averaged pitch angle and energy diffusion rates by first computing the weighted average of the diffusion coefficients over f_{pe}/f_{ce}^{eq} in each geomagnetic activity and spatial location bin. Next, the resulting latitudinally restricted bounce averaged diffusion coefficients from each latitude bin are summed to form the bounce averaged diffusion coefficients. Finally, the diffusion coefficients are drift averaged by averaging the bounce averaged coefficients over the 24 MLT bins. The resulting bounce and drift averaged pitch angle and energy diffusion coefficients, $\langle D_{\alpha\alpha}\rangle^D$ and $\langle D_{EE}\rangle^D$, respectively, are functions of energy, pitch angle, L^* and Kp. Bounce and drift averaged chorus diffusion coefficients capturing the effects of small and large WNA chorus are obtained by adding the two respective bounce and drift averaged diffusion coefficients.

For Kp $\geq$ 5, we do not have full MLT data coverage for $L^* \geq 4$ and therefore have to take special measures when drift averaging in order to obtain diffusion coefficients that represent the observed chorus wave intensity. For $L^* = 4$ and $L^* = 5$, there is insufficient data in one MLT bin on the morning side, where chorus is typically observed, for good statistics. We exclude this MLT bin in the drift averaging and average over 23 MLT bins instead. For $L^* = 5.5$, there are insufficient observations over a wide range of MLT bins and we use the bounce and drift averaged diffusion coefficients for $L^* = 5$ when Kp $\geq$ 5. Similarly, for $L^* = 6.0$ full MLT coverage is not available for Kp $\geq$ 1, and we use the bounce and drift averaged diffusion coefficients for $L^* = 5.5$, including the modification for Kp $\geq$ 5 mentioned above, for all activity bins with Kp $\geq$ 1. Inclusion of additional data sets, such as those from Arase or THEMIS, will be required to fully extend the diffusion coefficients to higher L^*.

4.2. Bounce Averaged Diffusion Coefficients

Figure 10 shows the bounce averaged chorus pitch angle diffusion coefficients for Kp $\geq$ 5 at $L^* = 4.5$ for increasing MLT, left to right, and increasing energy, from bottom to top, for the low WNA chorus (orange), high WNA chorus (pink), and the two combined (purple). In most MLT sectors, low WNA chorus has the dominant contribution to the combined WNA diffusion coefficients across all energies and pitch angles. However, between $4 \leq$ MLT < 11 at intermediate pitch angles high WNA chorus can give large diffusion rates. At MLT = 4.5, this is observed for energies $E \leq 1$ MeV, while for MLT = 7.5 and MLT = 11.5, the contribution from high WNA chorus is mostly observed at the higher energies $E \geq 500$ keV. In sectors MLT = 1.5 and MLT = 4.5, high WNA chorus can also be seen to increase the diffusion rates for energies $E \leq 100$ keV at large pitch angles $\alpha > 75°$.

Figure 11 shows the comparison of the bounce averaged chorus pitch angle diffusion coefficients, computed by combining the small and large WNA chorus diffusion coefficients, with two existing diffusion coefficient matrices, in the same format as Figure 10. We compare our results with the chorus diffusion coefficients computed in Horne et al. (2013), labeled by Horne 2013, and the chorus diffusion coefficients computed using the data in Meredith et al. (2020), labeled Meredith 2020, for Kp = 5 and $L^* = 4.0$. The Horne 2013 and Meredith 2020 diffusion coefficients use the Olson and Pfitzer (1977) external magnetic field model and were computed using average values of chorus wave intensity and f_{pe}/f_{ce} in each activity and spatial location bin. Both assumed the field aligned WNA distribution adopted in Horne et al. (2013). While the coefficients in Horne et al. (2013) assumed a Gaussian form for the wave spectra, Meredith 2020 used the data-driven version of PADIE (Glauert & Horne, 2005) allowing the wave spectra to be derived directly from the data without additional fitting. Since the three diffusion coefficient matrices adopt different bins for Kp, the coefficients shown for Kp = 5 are those for the Kp bin that contains Kp = 5. More explicitly, for the Horne 2013 we use the coefficients from the Kp $\geq$ 4 bin, for Meredith 2020 those from $4 \leq$ Kp < 7 and for the diffusion coefficients presented here we take the Kp $\geq$ 5 bin.

For MLT = 1.5 and energies $E = 500$ keV and $E = 1$ MeV, panels (q) and (i) respectively, we observe that the new diffusion coefficients and Meredith 2020 have a similar in profile in pitch angle, with the results presented here

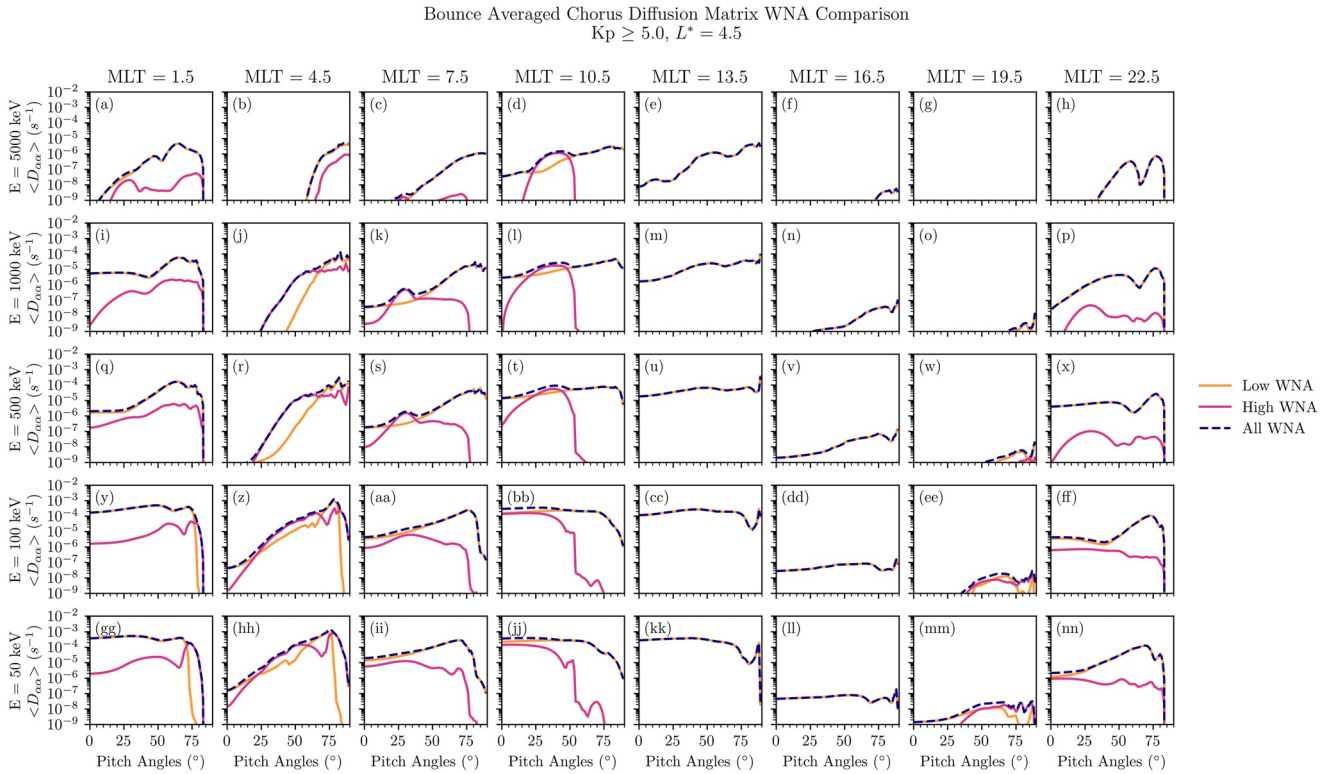

Figure 10. Comparison of bounce averaged chorus wave pitch angle diffusion coefficients for low and high wave normal angle (orange and pink, respectively), and the two combined (purple), for Kp ≥ 5 and L^* = 4.5. MLT, denoted by the midpoint of each 1 hour MLT bin, increases from left to right and energy increases from bottom to top.

giving rise to diffusion rates that are typically a factor of 3–6 times larger at low to intermediate pitch angles. In this region the new diffusion coefficients would result in more diffusion into the loss cone and hence more losses due to waves at high latitudes (Wang & Shprits, 2019). On the other hand, the Horne 2013 pitch angle diffusion coefficients decrease with decreasing pitch angle for pitch angles $\alpha < 40°$. This pattern is also observed in other MLT sectors for Horne 2013. The differences between the Horne 2013 results and the Meredith 2020 results are most likely due to the difference in wave models. The VLF database used to compute the Meredith 2020 diffusion coefficients included an additional ∼6 years of data from three THEMIS spacecraft and 3 years of data from Van Allen probes A and B, greatly improving the coverage and statistics in the near equatorial region (Meredith et al., 2020). The absence of the new diffusion coefficients at MLT = 4.5 is due to insufficient data coverage in this high activity bin to exceed the required threshold of 100 samples for adequate statistics. For Meredith 2020, diffusion coefficients are absent at MLT = 16.5 and MLT = 19.5 as these bins have been identified as being inside the plasmapause.

In the morning sector at MLT = 7.5, the new diffusion coefficients are higher compared with both existing diffusion coefficient matrices across all energies and the majority of pitch angles. On the dayside at MLT = 10.5, the new results and Meredith 2020 are comparable at energies $E \leq 100$ keV, but deviate at the higher energies for low pitch angles. This can be seen for MLT = 13.5 as well, where Meredith 2020 has higher pitch angle diffusion coefficients for energies E = 500 keV and E = 1 MeV at low to intermediate pitch angles. This suggests that the chorus wave intensity at high latitudes derived from mapping Van Allen Probe observations with the VLF database latitude profile does not capture all the wave intensity observed at high latitudes in the Meredith et al. (2020) database due to the presence of wave intensity above the mapped equatorial gyrofrequency at high latitudes. A similar difference is seen on the nightside at MLT = 22.5, however, as there is no mapping to higher latitudes on the nightside at $L^* \geq 4.0$, as discussed in Section 2.4, this is expected. The diffusion coefficients for E = 1 MeV, where the difference is largest, are of order 10^{-7} s^{-1} at low pitch angles for Meredith 2020, and therefore relatively low.

The comparison of bounce averaged energy diffusion coefficients, in the same format as Figure 11, is shown in Figure 12. Similar trends to those observed in the pitch angle diffusion coefficients can be seen in the energy

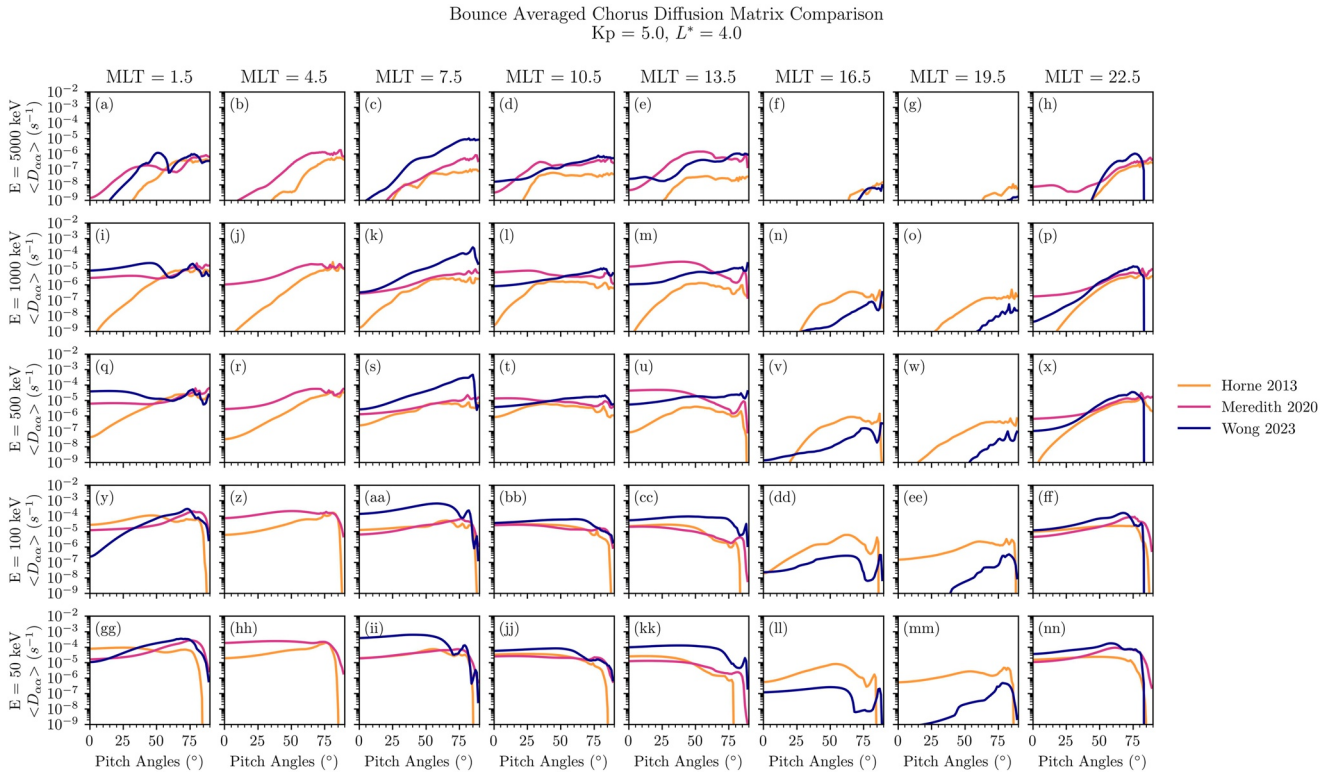

Figure 11. Comparison of bounce averaged chorus wave pitch angle diffusion coefficients with Horne et al. (2013), labeled Horne 2013, and chorus diffusion coefficients derived from the data in Meredith et al. (2020), labeled Meredith 2020, for Kp = 5 and L^* = 4.0. MLT, denoted by the midpoint of each 1 hour MLT bin, increases from left to right and energy increases from bottom to top.

diffusion coefficients. In general there is a remarkable similarity to the previous Horne 2013 and Meredith 2020 results. One notable difference is at 1.5 MLT where the energy diffusion rates at 500 and 1,000 keV are higher than the previous models at small and intermediate pitch angles. For these same energies at MLT = 13.5, the pitch angle diffusion coefficients for Meredith 2020 were significantly larger than those presented here at low pitch angles, while the energy diffusion coefficients show almost negligible differences. On the other hand, significant differences are still seen in the energy diffusion coefficients for MLT = 22.5 where the Meredith 2020 energy diffusion coefficients are small but signficantly larger than those of the new results.

4.3. Bounce and Drift Averaged Diffusion Coefficients

The bounce and drift averaged chorus diffusion coefficients capturing both small and large WNA are shown in Figure 13 for quiet activity, $0 \leq Kp < 1$, and active times, $Kp \geq 5$, for different L^* values. The bold labels for panels (l) and (p) are to indicate that the diffusion coefficients shown for $L^* = 6.0$ have been taken to be the same as $L^* = 5.5$, due to insufficient MLT data coverage during active conditions. The diffusion coefficients increase with increasing Kp and shift down to lower L^* values for high activity levels due to the erosion of the plasmasphere.

Figure 14 shows the comparison of the bounce and drift averaged pitch angle diffusion coefficients constructed in this paper with the existing chorus diffusion coefficients in Horne et al. (2013), labeled Horne 2013, and the diffusion coefficients derived from the database in Meredith et al. (2020), labeled Meredith 2020. We compare the three diffusion coefficient matrices at Kp = 5 for five energies from 50 keV to 5 MeV, and six L^* values increasing from left to right. From the figure it is evident that at $L^* = 3.0$ the new results have higher pitch angle diffusion coefficients across all energies for pitch angles $\alpha < 65°$ compared with Horne 2013. The Meredith 2020 diffusion coefficients are absent for this L^* value as it has identified this L^* value to be inside the plasmapause. At $L^* = 4.0$, the new diffusion coefficients exceed the diffusion rates in Horne 2013 for most pitch angles for all energies and exceed the Meredith 2020 diffusion coefficients at large pitch angles for all energies. The increase

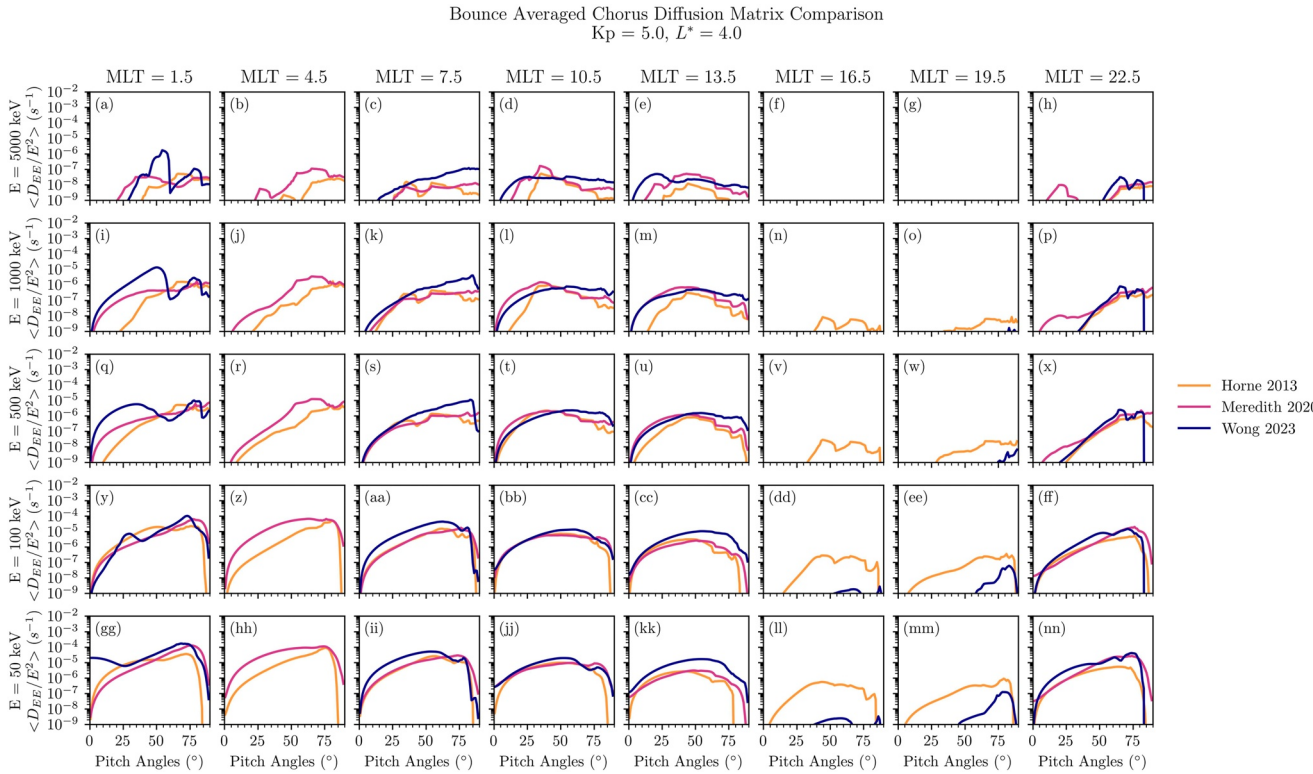

Figure 12. Comparison of bounce averaged chorus wave energy diffusion coefficients with Horne et al. (2013), labeled Horne 2013, and chorus diffusion coefficients derived from the data in Meredith et al. (2020), labeled Meredith 2020, for Kp = 5 and L^* = 4.0. MLT, denoted by the midpoint of each 1 hour MLT bin, increases from left to right and energy increases from bottom to top.

in the diffusion coefficients at low L^* during active conditions can be attributed to the use of TS04 in the computation of the new coefficients which shifts the chorus wave intensity to lower L^* values, as seen in Figure 1, and the use of the ECH criterion to identify chorus outside the plasmapause. The diffusion rates are generally higher near the loss cone than in Horne 2013. Finally, at $L^* \geq 5.0$ the profile of the diffusion coefficients in pitch angle is most similar to those in Meredith 2020.

Figure 15 shows the bounce and drift averaged energy diffusion coefficients in the same format as Figure 14. At $L^* = 3$ the new diffusion coefficients have higher diffusion rates, typically by factors of 2–10, when compared with Horne 2013 for all pitch angles at energies of 500 keV and above. At $L^* = 3.5$ the new bounce and drift average energy diffusion coefficients are typically factors of 3–10 times larger than those in Meredith 2020. Further out at $L^* = 4.0$ the differences are not so great and are larger typically by factors of 2–4. For $L^* > 4$, the three diffusion coefficient matrices are very similar for $E \leq 500$ keV. At $E = 1$ MeV, both the new diffusion coefficients and Horne 2013 have lower energy diffusion coefficients at lower pitch angles compared with Meredith 2020, suggesting that the Meredith 2020 diffusion coefficients have larger contributions from high latitude chorus waves. The use of TS04 in the new diffusion coefficients also contributes to the lower diffusion at higher L^*, as the chorus wave intensity shifts to lower L^* during active conditions when using TS04.

5. Discussion

From the comparison in Figures 14 and 15 the differences between the chorus diffusion coefficients developed in this paper and existing diffusion coefficients are typically an order of magnitude or less. However, it has been shown that low plasma density conditions can significantly increase chorus acceleration of MeV electrons to ultrarelativistic energies (Agapitov et al., 2019; Allison et al., 2021; Horne, Thorne, Shprits, et al., 2005). This suggests that the current formulation, which averages over the diffusion coefficients in different f_{pe}/f_{ce}^{eq} bins, does not fully capture the effects of chorus during extreme plasma density depletions. In Figure 16 we plot the bounce and drift averaged chorus pitch angle and energy diffusion coefficients in the nine f_{pe}/f_{ce}^{eq} bins and

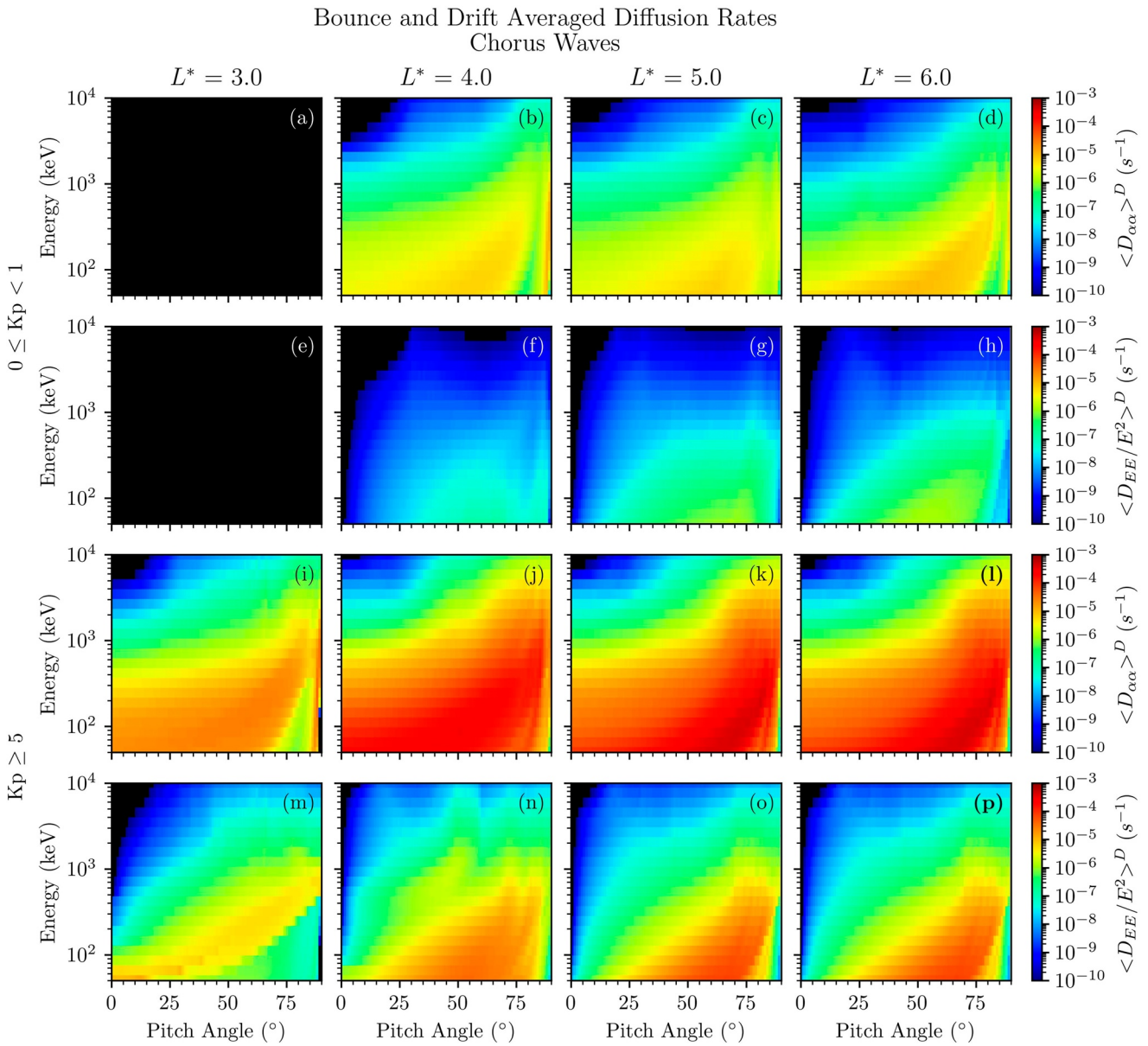

Figure 13. Bounce and drift averaged chorus wave pitch angle and energy diffusion coefficients for, from left to right, increasing L^* for low and high Kp ranges. The bold labels for panels (l) and (p) at $L^* = 6.0$ and Kp ≥ 5 denotes the fact that these diffusion coefficients have been taken to be the same as $L^* = 5.5$, due to insufficient MLT data coverage.

averaged across all f_{pe}/f_{ce}^{eq} bins for Kp ≥ 5 and $L^* = 4.5$. The average across all f_{pe}/f_{ce}^{eq} is computed as a sample size weighted average and therefore the average can be dominated by f_{pe}/f_{ce}^{eq} bins with low diffusion rates but a large number of samples. As can be seen from the figure, the diffusion coefficients can be close to an order of magnitude larger in the $2.53 \leq f_{pe}/f_{ce}^{eq} < 3.19$ bin for high energy electrons across a range of pitch angles compared to the average over all f_{pe}/f_{ce}^{eq} bins. Hence diffusion in regions of low f_{pe}/f_{ce}^{eq} could be up to ~100 times larger than the diffusion coefficients in Horne 2013 and Meredith 2020 and significantly affect acceleration and loss rates.

In particular, at $E = 5$ MeV, the pitch angle diffusion coefficients for $2.53 \leq f_{pe}/f_{ce}^{eq} < 3.19$ are larger and extend into the loss cone compared with the other f_{pe}/f_{ce} bins and the sample size weighted average, which could result in increased losses of high energy electrons. Low values of f_{pe}/f_{ce}^{eq} have higher occurrence rates in the pre-dawn sector 0–6 MLT (Agapitov et al., 2019), where the methods used to compute the low WNA diffusion coefficients

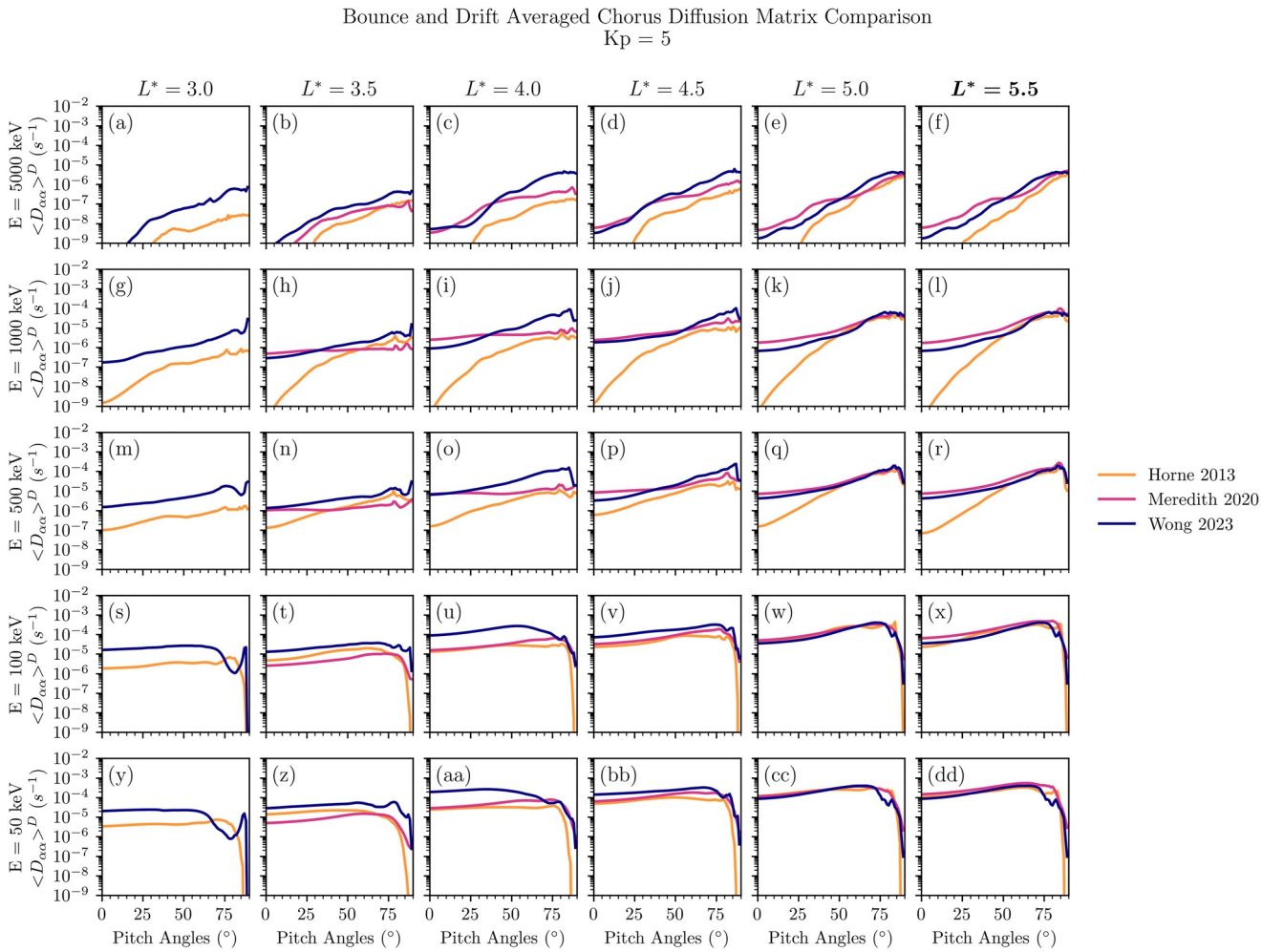

Figure 14. Comparison of bounce and drift averaged chorus wave pitch angle diffusion coefficients with Horne 2013 and Meredith 2020 for Kp = 5 for, from left to right, increasing L^* and, bottom to top, increasing energy. The bold text for the column at $L^* = 5.5$ denotes the fact that the value of the diffusion coefficients at $L^* = 5.5$ have been taken to be the same as $L^* = 5.0$, due to insufficient MLT data coverage.

either do not extend to magnetic latitudes beyond the Van Allen probes coverage, or only use wave observations within $|\lambda| < 10°$. These restrictions will affect the diffusion coefficients at low f_{pe}/f_{ce}^{eq}, and a more detailed comparison of the diffusion coefficients arising from different f_{pe}/f_{ce}^{eq} ranges requires knowledge of the wave intensity and f_{pe}/f_{ce} at higher latitudes.

We note that the determination of f_{pe} and hence f_{pe}/f_{ce}^{eq} is challenging in the plasma trough where the densities are low. Here the plasma frequency is estimated from either the lower frequency limit of the plasma continuum or from the upper hybrid frequency determined from the brightest $(n + 1/2)f_{ce}$ emission above the $3/2f_{ce}$ emission (Kurth et al., 2015). However, the former is an upper limit to f_{pe} and the latter is sometimes difficult to identify, and, even when correctly identified is uncertain by an order of f_{ce}. Thus the true value of f_{pe} can be lower than the value estimated in the Level 4 data product. This would result in a lower value of f_{pe}/f_{ce}^{eq} and increase the diffusion rates.

The choice of external magnetic field model has also been shown to have a significant impact on the chorus diffusion coefficients at lower L^*. Figure 17 shows the L^* profile of the bounce and drift averaged diffusion coefficients of Horne 2013, Meredith 2020 and the new results at Kp = 5 for $E = 1$ MeV, and two pitch angles $\alpha = 45°$ and $\alpha = 75°$. The figure shows higher energy diffusion coefficients for the results presented here computed using TS04 compared with the existing Olson-Pfitzer based diffusion coefficients for $L^* < 4.5$ for $\alpha = 45°$. The diffusion coefficients in panel (a) peak at $L^* = 4.0$. For $\alpha = 75°$, the energy diffusion coefficients are larger than the Horne 2013 and Meredith 2020 diffusion coefficients for all L^*, but show the largest differences at $L^* = 3.0$ and $L^* = 4.0$. As shown in Figure 1 the Van Allen probes sample lower L^* using TS04 during active periods. The

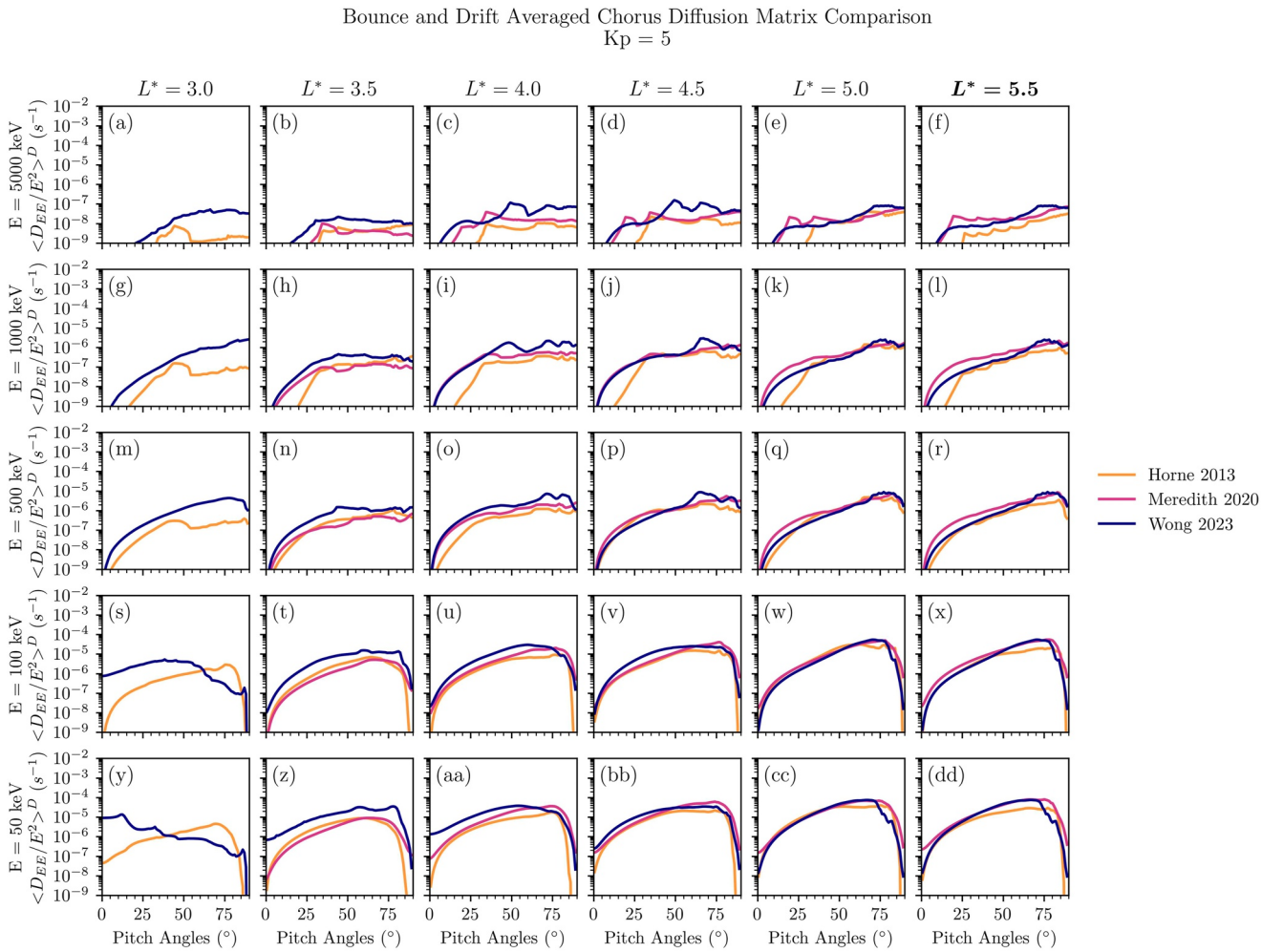

Figure 15. Comparison of bounce and drift averaged chorus wave energy diffusion coefficients with Horne 2013 and Meredith 2020 for Kp = 5 for, from left to right, increasing L^* and, bottom to top, increasing energy. The bold text for the column at $L^* = 5.5$ denotes the fact that the value of the diffusion coefficients at $L^* = 5.5$ have been taken to be the same as $L^* = 5.0$, due to insufficient MLT data coverage.

blue asterisks at $L^* = 5.5$ and $L^* = 6.0$ are to highlight that the diffusion coefficient values shown are obtained by assuming the values at $L^* = 5.0$, where there is sufficient MLT coverage.

For the computation of the lower hybrid resonance in both the Van Allen probes data and the VLF database we use the high density approximation, which can neglect wave intensity in the lowest frequency band when the density is low. This problem is especially pronounced at high latitudes, but as the Van Allen probes orbit is near equatorial, the average chorus wave intensity missed in this analysis is 0.59 pT^2 for $|\lambda| > 18°$, corresponding to 0.16%, and is less for lower magnetic latitudes. Using the density measurements from Cluster we computed the percentage error in the lower hybrid resonance frequency derived using the high density approximation and found the error to be largest at high latitudes between $22 \leq \text{MLT} < 6$. The resulting average chorus wave intensity not accounted for, including times when no chorus waves are observed, is 15.3 pT^2 for $30° \leq |\lambda| < 45°$ and 50.7 pT^2 $45° \leq |\lambda| < 60°$, which corresponds to 3.4% and 14.6%, respectively. This suggests a non-negligible proportion of wave intensity for lower band chorus at high latitudes can be omitted when using the high density approximation to compute the lower hybrid resonance which would be interesting to investigate in future studies.

6. Conclusions

We have computed bounce and drift averaged chorus diffusion with coefficients for $3.0 < L^* < 6.0$, using the TS04 external magnetic field model, taking into account co-located measurements of the chorus magnetic field intensity and f_{pe}/f_{ce}, by combining the Van Allen probes measurements with data from the VLF database in

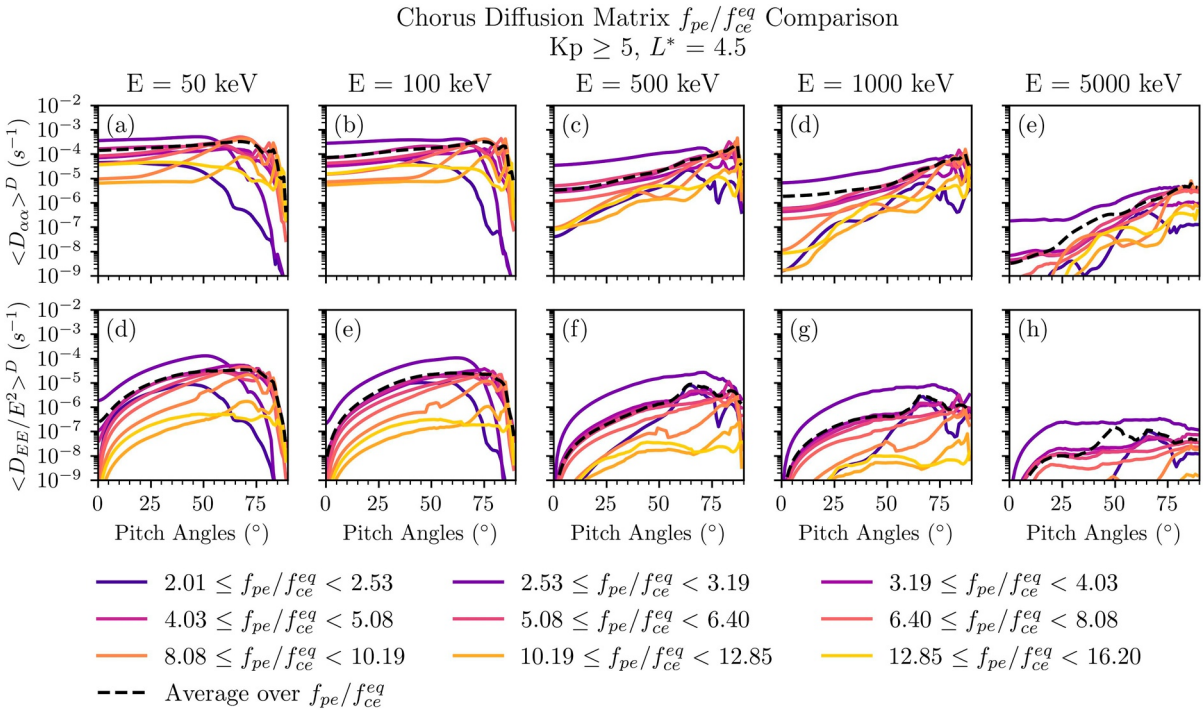

Figure 16. Bounce and drift averaged chorus pitch angle and energy diffusion in nine f_{pe}/f_{ce}^{eq} bins and the sample size weighted average across all f_{pe}/f_{ce}^{eq} bins for $L^* = 4.5$ and Kp ≥ 5.

Meredith et al. (2020). The results also take into account the variation of chorus WNA with spatial location and f_{pe}/f_{ce}, and detailed comparisons between the new diffusion coefficients and two existing chorus diffusion coefficient matrices have been performed to highlight the key differences. Our principal findings are:

1. In most MLT sectors chorus propagating at small WNAs has the dominant contribution to the diffusion rates. However, in the region 4 ≤ MLT < 11 high WNAs dominate the pitch angle diffusion coefficients at intermediate pitch angles.
2. Bounce and drift averaged pitch angle and energy diffusion rates during active conditions in the region 3.0 < L^* < 4.0 are primarily larger than those in Horne 2013 and Meredith 2020 by up to a factor of 10 depending on energy and pitch angle.

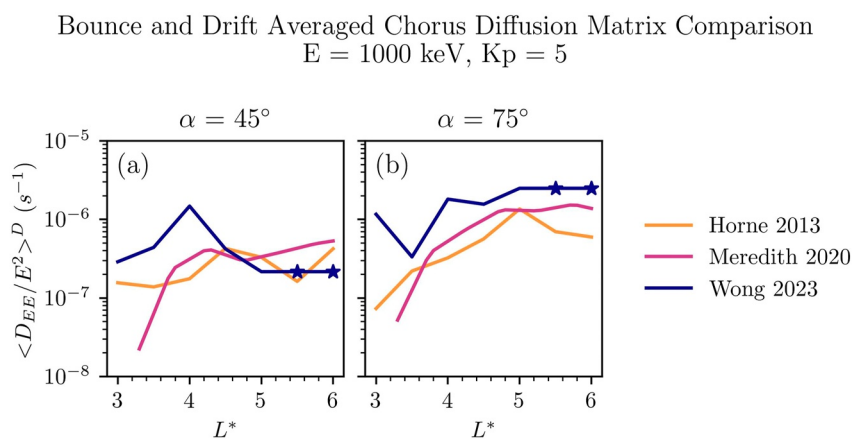

Figure 17. Comparison of the variation of bounce and drift averaged chorus energy diffusion coefficients with L^* for Horne et al. (2013), labeled Horne 2013, chorus diffusion coefficients derived from the data in Meredith et al. (2020), labeled Meredith 2020, and the diffusion coefficients presented here for Kp = 5, E = 1,000 keV for pitch angles 45° and 75°. The blue asterisk for Wong 2023 at $L^* = 5.5$ and $L^* = 6.0$ denotes the fact that these diffusion coefficients have been taken to be the same as $L^* = 5.0$, due to insufficient MLT data coverage.

3. Further out, in the region $4.5 < L^* < 5.0$, the bounce and drift averaged pitch angle and energy diffusion rates during active conditions computed by the new method are similar to those in Meredith 2020.
4. The bounce and drift averaged energy and pitch angle diffusion rates can be significantly larger than our model in regions of low f_{pe}/f_{ce}^{eq}, where the differences can be up to a factor of 10 depending on energy and pitch angle.

The new diffusion rates will be incorporated into the BAS Radiation Belt Model (Glauert et al., 2014, 2021) leading to more accurate space weather models and forecasts.

Appendix A: Mapping VLF Latitude Profiles to Equator

This section describes the method used for mapping the chorus wave intensity binned in $0.1f_{ce}$ frequency bands in the existing multi-satellite VLF database to $0.1f_{ce}^{eq}$ frequency bands, assuming a dipole field. In each activity, L^*, MLT, and λ bin the database contains the average chorus wave intensity in each $0.1f_{ce}$ frequency band. To rebin the wave magnetic field intensity into frequency bands in terms of f_{ce}^{eq}, an assumption has to be made regarding how the wave intensity in a f_{ce} frequency band is distributed over the f_{ce}^{eq} bands it maps back to. The simplest choice would be to assume the wave intensity is distributed uniformly over the corresponding f_{ce}^{eq} bands, however, this can result in too much intensity being allocated to the higher equatorial frequencies. One other choice would be to use the equatorial distribution of wave intensity with frequency. To be as general as possible, we denote the fraction of intensity distributed to equatorial frequency band i, as A_i, where $\sum_i A_i = 1$. In each activity, L^*, MLT and λ bin we identify the highest f_{ce} frequency band that can contribute to the equatorial spectrum at that latitude. Starting from this highest band and working down to the lowest f_{ce} frequency band we derive the equatorial spectrum resulting from each f_{ce} band, m, in the following way:

1. Using the limits of band m, $(0.1mf_{ce}, 0.1(m+1)f_{ce})$, compute the overlap, $x_{i,m}$, with equatorial frequency band i, with limits $(0.1if_{ce}^{eq}, 0.1(i+1)f_{ce}^{eq})$. This can be achieved by first computing

$$\begin{aligned} a &= \max\left(0.1if_{ce}^{eq}, 0.1mf_{ce}\right) \\ b &= \min\left(0.1(i+1)f_{ce}^{eq}, 0.1(m+1)f_{ce}\right) \end{aligned} \tag{A1}$$

Then we have

$$x_{i,m} = \begin{cases} (b-a)/0.1f_{ce}, & \text{if } a < b \\ 0, & \text{otherwise} \end{cases} \tag{A2}$$

The division by $0.1f_{ce}$ corresponds to the width of frequency band m, and for the lowest frequency band would instead be $0.1f_{ce} - f_{LHR}$. Repeating for all equatorial frequency bands gives overlaps satisfying $\sum_i x_{i,m} = 1$.

1. Let the average wave intensity in band m be B_m. The fraction of wave intensity mapped to equatorial band i, $B_{i,m}$, is then given by

$$B_{i,m} = \frac{x_{i,m}A_i}{\sum_i x_{i,m}A_i} B_m \tag{A3}$$

This procedure ensures the wave intensity assigned to each equatorial frequency band is weighted by the overlap with local frequency band m and also the assumed distribution of intensity, given by the A_i. Repeating this procedure for each local frequency band, the total chorus wave intensity for equatorial frequency band i, B_i, in this activity and location bin is then given by $\sum_m B_{i,m}$. In the simplest case of the uniform distribution of intensity Equation A3 reduces to

$$B_{i,m} = x_{i,m}B_m. \tag{A4}$$

With the average chorus wave intensity in terms of f_{ce}^{eq} frequency bins, we can determine the variation of each equatorial frequency bin with magnetic latitude.

In this paper, we use the equatorial wave spectra in the VLF database within $|\lambda| \leq 3°$ in 2 hr MLT bins, $2L^*$ bins $2 \leq L^* < 4$ and $4 \leq L^* < 6$, and 5 Kp bins $0 \leq \text{Kp} < 1$, $1 \leq \text{Kp} < 2$, $2 \leq \text{Kp} < 3$, $3 \leq \text{Kp} < 4$, and $\text{Kp} \geq 4$ to

determine the A_i in the mapping. Using the same spatial and activity bins as for determining A_i we compute a profile for how the wave intensity in each frequency band varies with absolute latitude in 3° latitude bins from the equator to 60° magnetic latitude.

Appendix B: Wave Normal Angle Distribution Parameters

Tables B1–B7 contain the mean, ψ_m, and standard deviation, σ, of the Gaussian fits,

$$g(\psi) = \frac{1}{\sqrt{2\pi}\sigma}\exp\left(-\frac{(\psi-\psi_m)^2}{2\sigma^2}\right) \tag{B1}$$

of the probability density functions of the wave normal angle (WNA) in each spatial location and f_{pe}/f_{ce}^{eq} bin.

Table B1
Lower Band Chorus Wave Normal Angle Distribution Single Gaussian Fit Parameters (ψ_m, σ) for Distributions With a Single Peak

	$0° \le \lvert\lambda\rvert < 6°$	$6° \le \lvert\lambda\rvert < 12°$	$12° \le \lvert\lambda\rvert < 18°$	$\lvert\lambda\rvert \ge 18°$
$0 \le$ MLT < 1	–	–	–	(25.22°, 21.34°)
$1 \le$ MLT < 2	–	–	–	(19.30°, 14.42°)
$2 \le$ MLT < 3	–	–	–	(20.78°, 16.84°)
$3 \le$ MLT < 4	–	–	–	(17.36°, 16.76°)
$4 \le$ MLT < 5	–	–	–	(18.05°, 13.66°)
$5 \le$ MLT < 6	–	–	–	(18.15°, 12.49°)
$6 \le$ MLT < 7	–	–	–	(17.35°, 13.82°)
$7 \le$ MLT < 8	–	–	–	–
$8 \le$ MLT < 9	(13.41°, 7.38°)	–	–	–
$9 \le$ MLT < 10	(12.75°, 6.74°)	(16.97°, 8.86°)	–	–
$10 \le$ MLT < 11	(12.53°, 6.13°)	(15.92°, 8.65°)	(16.86°, 11.39°)	–
$11 \le$ MLT < 12	(12.19°, 5.49°)	(15.00°, 7.73°)	(17.31°, 10.00°)	(17.76°, 11.71°)
$12 \le$ MLT < 13	(11.96°, 5.47°)	(14.82°, 6.99°)	(19.54°, 10.05°)	(17.56°, 10.33°)
$13 \le$ MLT < 14	(11.43°, 4.99°)	(16.64°, 7.50°)	(19.64°, 10.05°)	(18.55°, 10.66°)
$14 \le$ MLT < 15	(11.32°, 5.08°)	(18.25°, 8.40°)	(22.18°, 10.89°)	(19.51°, 9.98°)
$15 \le$ MLT < 16	(11.20°, 5.08°)	(17.61°, 7.83°)	(23.91°, 11.43°)	(24.11°, 12.47°)
$16 \le$ MLT < 17	(11.66°, 5.33°)	(19.69°, 8.48°)	(28.73°, 12.46°)	(27.05°, 15.22°)
$17 \le$ MLT < 18	(11.56°, 5.21°)	(18.22°, 6.78°)	(27.41°, 13.81°)	(38.46°, 14.58°)
$18 \le$ MLT < 19	(12.17°, 5.52°)	(18.03°, 7.93°)	(25.54°, 12.74°)	(31.42°, 18.39°)
$19 \le$ MLT < 20	(12.39°, 6.19°)	(20.85°, 10.07°)	(23.74°, 12.10°)	(30.93°, 13.13°)
$20 \le$ MLT < 21	(11.37°, 6.37°)	(18.55°, 11.80°)	(18.65°, 12.05°)	(25.90°, 14.17°)
$21 \le$ MLT < 22	–	–	(22.08°, 15.53°)	(26.01°, 11.93°)
$22 \le$ MLT < 23	–	–	(20.38°, 14.63°)	(22.03°, 16.17°)
$23 \le$ MLT < 24	–	–	(16.86°, 12.39°)	(25.22°, 21.74°)

Table B2
Lower Band Chorus Wave Normal Angle (WNA) Distribution Gaussian Fit Parameters (ψ_m, σ) for Distributions Exhibiting Two Peaks Dependent on L and f_{pe}/f_{ce}^{eq} for $0° \le |\lambda| < 12°$*

		$1 \le f_{pe}/f_{ce}^{eq} < 3.19$	$3.19 \le f_{pe}/f_{ce}^{eq} < 8.08$	$8.08 \le f_{pe}/f_{ce}^{eq} < 16.20$	$16.20 \le f_{pe}/f_{ce}^{eq} < 41$
$0° \le \|\lambda\| < 6°$	$2.25 \le L^* < 3.25$	(13.67°, 8.62°)	(11.37°, 11.02°)	(18.79°, 13.06°)	–
$21 \le MLT < 8$		(14.42°, 7.43°)			
	$3.25 \le L^* < 4.25$	**(58.13°, 7.07°)**	(13.32°, 9.67°)	(14.85°, 10.04°)	(19.47°, 14.33°)
		$\psi_{sep} = 43.5°$			
		(17.38°, 9.91°)	(16.38°, 8.26°)		
	$4.25 \le L^* < 5.25$	**(61.19°, 7.76°)**	**(58.91°, 9.51°)**	(11.58°, 6.67°)	(11.40°, 7.51°)
		$\psi_{sep} = 37.5°$	$\psi_{sep} = 37.5°$		
		(18.88°, 9.66°)	(16.96°, 10.13°)	(14.15°, 7.58°)	
	$5.25 \le L^* < 6.25$	**(65.31°, 5.83°)**	**(63.92°, 6.95°)**	**(62.15°, 9.05°)**	(11.93°, 8.16°)
		$\psi_{sep} = 34.5°$	$\psi_{sep} = 40.5°$	$\psi_{sep} = 40.5°$	
$6° \le \|\lambda\| < 12°$	$2.25 \le L^* < 3.25$	(17.92°, 10.24°)	(22.67°, 14.57°)	(20.45°, 15.08°)	(8.10°, 3.89°)
$21 \le MLT < 9$		(18.72°, 9.71°)	(18.87°, 11.57°)		
	$3.25 \le L^* < 4.25$	**(63.46°, 7.21°)**	**(62.18°, 7.05°)**	(19.52°, 13.54°)	(30.98°, 14.87°)
		$\psi_{sep} = 49.5°$	$\psi_{sep} = 52.5°$		
		(17.89°, 10.31°)	(17.38°, 9.10°)	(17.15°, 11.91°)	
	$4.25 \le L^* < 5.25$	**(67.82°, 6.22°)**	**(65.75°, 7.11°)**	**(66.67°, 7.11°)**	(27.42°, 16.18°)
		$\psi_{sep} = 46.5°$	$\psi_{sep} = 46.5°$	$\psi_{sep} = 49.5°$	
		(13.98°, 8.70°)	(15.81°, 8.42°)	(21.23°, 12.75°)	(11.17°, 6.62°)
	$5.25 \le L^* < 6.25$	**(70.82°, 5.05°)**	**(68.02°, 5.49°)**	**(65.90°, 8.05°)**	**(61.94°, 7.28°)**
		$\psi_{sep} = 43.5°$	$\psi_{sep} = 43.5°$	$\psi_{sep} = 46.5°$	$\psi_{sep} = 43.5°$

Note. The distributions highlighted in bold are considered as those with large WNA.

Table B3
Lower Band Chorus Wave Normal Angle (WNA) Distribution Gaussian Fit Parameters (ψ_m, σ) for Distributions Exhibiting Two Peaks Dependent on L and f_{pe}/f_{ce}^{eq} for $|\lambda| \ge 12°$*

		$1 \le f_{pe}/f_{ce}^{eq} < 3.19$	$3.19 \le f_{pe}/f_{ce}^{eq} < 8.08$	$8.08 \le f_{pe}/f_{ce}^{eq} < 16.20$	$16.20 \le f_{pe}/f_{ce}^{eq} < 41$
$12° \le \|\lambda\| < 18°$		(23.30°, 10.95°)			
$0 \le MLT < 10$					
	$2.25 \le L^* < 4.25$	**(68.74°, 6.70°)**	(29.87°, 20.80°)	(27.86°, 18.8°)	**(43.51°, 17.77°)**
		$\psi_{sep} = 55.5°$			
		(15.99°, 9.87°)	(16.61°, 9.79°)	(22.81°, 13.02°)	
	$4.25 \le L^* < 6.25$	**(71.88°, 6.77°)**	**(70.16°, 7.29°)**	**(73.65°, 7.42°)**	(41.45°, 14.19°)
		$\psi_{sep} = 52.5°$	$\psi_{sep} = 52.5°$	$\psi_{sep} = 55.5°$	
		(28.52°, 11.53°)	(31.95°, 15.62°)		
$\|\lambda\| \ge 18°$	$2.25 \le L^* < 4.25$	**(68.71°, 5.00°)**	**(70.22°, 6.23°)**	**(43.86°, 20.80°)**	(35.68°, 17.31°)
$7 \le MLT < 11$		$\psi_{sep} = 58.5°$	$\psi_{sep} = 61.5°$		
			(18.08°, 12.47°)		
	$4.25 \le L^* < 6.25$	(25.15°, 18.20°)	**(71.64°, 7.09°)**	**(46.85°, 27.98°)**	(38.46°, 13.29°)
			$\psi_{sep} = 55.5°$		

Note. The distributions highlighted in bold are considered as those with large WNA.

Table B4
Upper Band Chorus Wave Normal Angle (WNA) Distribution Gaussian Fit Parameters (ψ_m, σ) for $0° \le |\lambda| < 6°$

		$1 \le f_{pe}/f_{ce}^{eq} < 3.19$	$3.19 \le f_{pe}/f_{ce}^{eq} < 8.08$	$8.08 \le f_{pe}/f_{ce}^{eq} < 41$
$0 \le$ MLT < 6			(7.34°, 6.69°)	(3.63°, 3.84°)
	$2.25 \le L^* < 3.25$	**(47.99°, 9.12°)**	**(46.04°, 10.42°)**	**(49.42°, 6.53°)**
			$\psi_{sep} = 22.5°$	$\psi_{sep} = 37.5°$
	$4.25 \le L^* < 6.25$	**(41.86°, 17.26°)**	**(41.46°, 17.27°)**	(16.26°, 20.32°)
$6 \le$ MLT < 12		(13.47°, 8.81°)		
	$2.25 \le L^* < 3.25$	**(47.38°, 7.76°)**	(9.74°, 16.2°)	(5.24°, 4.81°)
		$\psi_{sep} = 28.5$		
	$4.25 \le L^* < 6.25$	**(39.91°, 14.87°)**	(32.71°, 19.02°)	(9.70°, 12.92°)
$12 \le$ MLT < 18	$2.25 \le L^* < 4.25$	–	(6.22°, 7.06°)	(5.04°, 3.85°)
			(7.03°, 6.17°)	
	$4.25 \le L^* < 6.25$	–	**(40.29°, 8.56°)**	(5.68°, 7.73°)
			$\psi_{sep} = 28.5°$	
$18 \le$ MLT < 24				(3.81°, 3.03°)
	$2.25 \le L^* < 4.25$	**(49.18°, 7.44°)**	(17.62°, 20.65°)	**(31.71°, 7.18°)**
				$\psi_{sep} = 19.5°$
		(12.97°, 5.37°)	(12.60°, 8.13°)	
	$4.25 \le L^* < 6.25$	**(48.81°, 12,87°)**	**(52.87°, 11.12°)**	(3.41°, 6.43°)
		$\psi_{sep} = 19.5°$	$\psi_{sep} = 25.5°$	

Note. The distributions highlighted in bold are considered as those with large WNA.

Table B5
Upper Band Chorus Wave Normal Angle (WNA) Distribution Gaussian Fit Parameters (ψ_m, σ) for $6° \le |\lambda| < 12°$

		$1 \le f_{pe}/f_{ce}^{eq} < 3.19$	$3.19 \le f_{pe}/f_{ce}^{eq} < 8.08$	$8.08 \le f_{pe}/f_{ce}^{eq} < 41$
$0 \le$ MLT < 6			(7.6°, 4.59°)	(6.29°, 5.67°)
	$2.25 \le L^* < 3.25$	**(55.95°, 7.58°)**	**(48.36°, 13.35°)**	**(52.04°, 7.71°)**
			$\psi_{sep} = 19.5°$	$\psi_{sep} = 37.5°$
		(17.91°, 10.28°)		(13.99°, 6.41°)
	$4.25 \le L^* < 6.25$	**(57.63°, 9.21°)**	**(56.65°, 11.28°)**	**(53.11°, 13.33°)**
		$\psi_{sep} = 34.5°$		$\psi_{sep} = 22.5°$
$6 \le$ MLT < 12				(9.34°, 10.12°)
	$2.25 \le L^* < 3.25$	**(55.19°, 8.58°)**	**(42.51°, 19.08°)**	**(47.06°, 7.99°)**
				$\psi_{sep} = 34.5°$
				(10.28°, 7.00°)
	$4.25 \le L^* < 6.25$	**(54.78°, 7.91°)**	**(49.81°, 11.90°)**	**37.47°, 10.03°**
				$\psi_{sep} = 25.5°$
$12 \le$ MLT < 18				(9.66°, 10.96°)
	$2.25 \le L^* < 4.25$	**(40.93°, 14.48°)**	(20.45°, 17.49°)	**(56.22°, 4.14°)**
				$\psi_{sep} = 49.5°$
			(16.19°, 8.32°)	
	$4.25 \le L^* < 6.25$	–	**(49.47°, 10.99°)**	(25.51°, 19.60°)
			$\psi_{sep} = 28.5°$	

Table B5
Continued

		$1 \le f_{pe}/f_{ce}^{eq} < 3.19$	$3.19 \le f_{pe}/f_{ce}^{eq} < 8.08$	$8.08 \le f_{pe}/f_{ce}^{eq} < 41$
$18 \le$ MLT < 24		(10.54°, 7.57°)	(12.56°, 9.72°)	(6.30°, 4.84°)
	$2.25 \le L^* < 4.25$	**(60.83°, 6.48°)**	**47.68°, 12.19°**	**(45.08°, 10.22°)**
		$\psi_{sep} = 25.5°$	$\psi_{sep} = 28.5°$	$\psi_{sep} = 25.5°$
		(14.20°, 10.35°)	(13.79°, 10.72°)	(8.82°, 8.67°)
	$4.25 \le L^* < 6.25$	**(63.59°, 7.54°)**	**(64.48°, 6.09°)**	**(54.78°, 9.78°)**
		$\psi_{sep} = 37.5°$	$\psi_{sep} = 40.5°$	$\psi_{sep} = 40.5°$

Note. The distributions highlighted in bold are considered as those with large WNA.

Table B6
Upper Band Chorus Wave Normal Angle (WNA) Distribution Gaussian Fit Parameters (ψ_m, σ) for $12° \le |\lambda| < 18°$

		$1 \le f_{pe}/f_{ce}^{eq} < 3.19$	$3.19 \le f_{pe}/f_{ce}^{eq} < 8.08$	$8.08 \le f_{pe}/f_{ce}^{eq} < 41$
$0 \le$ MLT < 6		(18.52°, 11.75°)	(12.66°, 9.74°)	(9.27°, 7.98°)
	$2.25 \le L^* < 3.25$	**(62.13°, 8.04°)**	**57.56°, 10.58°**	**60.91°, 7.52°**
		$\psi_{sep} = 40.5°$	$\psi_{sep} = 40.5°$	$\psi_{sep} = 49.5°$
		(17.99°, 12.00°)	(14.67°, 11.89°)	(17.80°, 8.94°)
	$4.25 \le L^* < 6.25$	**(65.58°, 8.30°)**	**(66.74°, 11.52°)**	**(66.39°, 9.88°)**
		$\psi_{sep} = 46.5°$	$\psi_{sep} = 40.5°$	$\psi_{sep} = 34.5°$
$6 \le$ MLT < 12			(17.71°, 11.82°)	
	$2.25 \le L^* < 3.25$	**(61.57°, 7.04°)**	**(58.14°, 9.27°)**	(15.61°, 19.76°)
			$\psi_{sep} = 37.5°$	
				(14.05°, 7.46°)
	$4.25 \le L^* < 6.25$	**(59.94°, 8.76°)**	**(55.41°, 14.22°)**	**(51.34°, 15.55°)**
				$\psi_{sep} = 28.5°$
$12 \le$ MLT < 18		(18.96°, 6.98°)	(22.24°, 12.35°)	
	$2.25 \le L^* < 4.25$	**(56.10°, 9.53°)**	**(57.46°, 7.99°)**	(9.95°, 9.56°)
		$\psi_{sep} = 28.5°$	$\psi_{sep} = 43.5°$	
			(22.14°, 9.51°)	(13.77°, 9.74°)
	$4.25 \le L^* < 6.25$	–	**(58.63°, 9.57°)**	**(55.90°, 12.82°)**
			$\psi_{sep} = 34.5°$	$\psi_{sep} = 34.5°$
$18 \le$ MLT < 24			(12.97°, 12.59°)	
	$2.25 \le L^* < 4.25$	(18.81°, 9.63°)	**(55.78°, 6.25°)**	(8.60°, 7.14°)
			$psi_{sep} = 46.5°$	
				(9.77°, 7.41°)
	$4.25 \le L^* < 6.25$	(13.65°, 11.17°)	(18.53°, 13.96°)	**(56.32°, 3.65°)**
				$\psi_{sep} = 49.5°$

Note. The distributions highlighted in bold are considered as those with large WNA.

Table B7
Upper Band Chorus Wave Normal Angle (WNA) Distribution Gaussian Fit Parameters (ψ_m, σ) for $|\lambda| \geq 18°$

		$1 \leq f_{pe}/f_{ce}^{eq} < 3.19$	$3.19 \leq f_{pe}/f_{ce}^{eq} < 8.08$	$8.08 \leq f_{pe}/f_{ce}^{eq} < 41$
$0 \leq$ MLT < 6	$2.25 \leq L^* < 3.25$	**(65.96°, 14.15°)**	(16.32°, 13.17°)	(15.13°, 12.15°)
			(19.32°, 14.10°)	
	$4.25 \leq L^* < 6.25$	(15.42°, 10.08°)	**(64.92°, 8.13°)**	(21.23°, 20.98°)
			$\psi_{sep} = 49.5°$	
$6 \leq$ MLT < 12		(21.17°, 11.46°)	(22.04°, 10.85°)	(16.73°, 11.31°)
	$2.25 \leq L^* < 3.25$	**(63.89°, 5.79°)**	**(63.32°, 9.07°)**	**(64.20°, 9.82°)**
		$\psi_{sep} = 43.5°$	$\psi_{sep} = 40.5°$	$\psi_{sep} = 46.5°$
		(17.20°, 13.30°)	(21.99°, 12.41°)	(15.67°, 8.61°)
	$4.25 \leq L^* < 6.25$	**(60.33°, 7.40°)**	**(65.31°, 7.55°)**	**(59.52°, 12.56°)**
		$\psi_{sep} = 46.5°$	$\psi_{sep} = 43.5°$	$\psi_{sep} = 34.5°$
$12 \leq$ MLT < 18	$2.25 \leq L^* < 4.25$	–	(35.30°, 21.20°)	–
	$4.25 \leq L^* < 6.25$	–	**(51.13°, 20.45°)**	(31.65°, 23.49°)
$18 \leq$ MLT < 24			(14.99°, 9.01°)	
	$2.25 \leq L^* < 4.25$	–	**(42.60°, 8.15°)**	(14.73°, 10.20°)
			$\psi_{sep} = 34.5°$	
			(20.11°, 11.63°)	
	$4.25 \leq L^* < 6.25$	–	**(68.20°, 9.8°)**	–
			$\psi_{sep} = 46.5°$	

Note. The distributions highlighted in bold are considered as those with large WNA.

Appendix C: Diffusion Coefficients Computation Method

The method used for computing the lower and upper band small WNA chorus diffusion coefficients depends on spatial region and are shown in Table C1. In Method 1, for each L^*, MLT, f_{pe}/f_{ce}^{eq} and Kp bin we compute bounce averaged diffusion coefficients for 20 magnetic latitude bins of width 3°, where the bounce average is over the latitude range of each latitude bin, between $0° \leq |\lambda| < 60°$ by mapping the Van Allen Probe observations using the method described in Section 2.4. Specifically, the chorus wave spectra is first mapped from frequency bands normalized to the local electron gyrofrequency bands to bands normalized to the equatorial electron gyrofrequency bands assuming a dipole field. Subsequently, for a magnetic latitude bin with midpoint $\hat{\lambda}$, we map the wave intensity, B_{obs}, of each observation in the L^*, MLT, f_{pe}/f_{ce}^{eq} and Kp bin to the derived wave intensity, $\hat{B}$, at $\hat{\lambda}$ using the VLF database magnetic latitude profiles. The diffusion coefficients for this magnetic latitude bin are then computed using the average wave intensity of the set of mapped wave intensities $\{\hat{B}\}$. Method 2 follows the same procedure as Method 1, except we only use Van Allen Probe observations with $|\lambda_{obs}| < 10°$. Finally, in Method 3 we use the chorus wave intensity in frequency bins relative to the local gyrofrequency and additionally bin measurements by absolute magnetic latitude in 3° bins. Bounce averaged diffusion coefficients are computed using the observations in each L^*, MLT, λ, f_{pe}/f_{ce}^{eq}, and Kp bin. As Method 3 does not use the VLF database derived magnetic latitude profiles, we are restricted to $|\lambda| < 21°$ in the regions where this method is applied.

Table C1
Methods Used for Computing Small Wave Normal Angle (WNA) Chorus Diffusion Coefficients Depending on Spatial Region

Band	Region	Method
Lower Band Chorus	$L^* < 4$ and $5 \leq$ MLT < 19	Method 1
	$L^* < 4$ and $19 \leq$ MLT < 5	Method 2
	$L^* \geq 4$ and $5 \leq$ MLT < 18	Method 1
	$L^* \geq 4$ and $18 \leq$ MLT < 5	Method 3
Upper Band Chorus	$L^* < 4$	Method 2
	$L^* \geq 4$ and $5 \leq$ MLT < 18	Method 2
	$L^* \geq 4$ and $18 \leq$ MLT < 5	Method 3

Ideally, we would only use Method 1 in computing the diffusion coefficients for small WNA chorus as it best captures the variability of f_{pe}/f_{ce}^{eq} and the effect of chorus at high latitudes. However, the magnetic latitude condition $|\lambda_{obs}| < 10°$ imposed in Method 2 is required in regions where lower and upper band chorus is often indistinguishable from background instrument noise at higher latitudes. The inclusion of these higher latitude measurements in the mapping results in lower than observed average wave intensity. Method 3 is required when the difference in the ratio B/B_{eq} between TS04 and the dipole field is large and the equatorial wave spectra derived using a dipole field is not a reasonable approximation, as detailed in Section 2.4. As the wave spectrum affects the energies the chorus waves are resonant with, and can therefore strongly influence the resulting diffusion coefficients, the chorus wave intensity is kept in terms of frequency bins relative to the local gyrofrequency and the mapping of observations to other latitudes is not performed. For lower and upper band large WNA chorus we only use Method 3 in computing the diffusion coefficients as these waves do not travel along magnetic field lines and may be strongly damped as they propagate to higher latitudes (Bortnik et al., 2006; Lauben et al., 2002). For all methods, the WNA distribution is uniquely determined by the spatial location and f_{pe}/f_{ce}^{eq} bin from Tables B1–B7.

Data Availability Statement

The results and data shown in this paper are available to download from the U.K. Polar Data Centre at https://doi.org/10.5285/fa63faf5-10d6-4c72-8b19-d41941f06812.

Acknowledgments
We acknowledge the NASA Van Allen probes and Craig Kletzing for use of the EMFISIS data, available online (https://emfisis.physics.uiowa.edu/data/index). We also acknowledge the Radiation Belt Storm Probes ECT Science Operations and Data Center for the provision of the magnetic ephemeris data, available online (https://www.rbsp-ect.lanl.gov/data-pub/rbspa/MagEphem/). We thank the NSSDC Omniweb for the provision of the Kp indices used in this paper. The research leading to these results has received funding from the Natural Environment Research Council (NERC) Highlight Topic Grant NE/P01738X/1 (Rad-Sat) and the NERC Grants NE/V00249X/1 (Sat-Risk), NE/R016038/1, and NE/X000389/1.

References

Agapitov, O. V., Artemyev, A., Krasnoselskikh, V., Khotyaintsev, Y. V., Mourenas, D., Breuillard, H., et al. (2013). Statistics of whistler mode waves in the outer radiation belt: Cluster staff-sa measurements. *Journal of Geophysical Research: Space Physics*, *118*(6), 3407–3420. https://doi.org/10.1002/jgra.50312

Agapitov, O. V., Mourenas, D., Artemyev, A., Claudepierre, S. G., Hospodarsky, G., & Bonnell, J. W. (2020). Lifetimes of relativistic electrons as determined from plasmaspheric hiss scattering rates statistics: Effects of ω_{pe}/ω_{ce} and wave frequency dependence on geomagnetic activity. *Geophysical Research Letters*, *47*(13), e2020GL088052. https://doi.org/10.1029/2020GL088052

Agapitov, O. V., Mourenas, D., Artemyev, A., Hospodarsky, G., & Bonnell, J. (2019). Time scales for electron quasi-linear diffusion by lower-band chorus waves: The effects of ω_{pe}/ω_{ce} dependence on geomagnetic activity. *Geophysical Research Letters*, *46*(12), 6178–6187. https://doi.org/10.1029/2019GL083446

Agapitov, O. V., Mourenas, D., Artemyev, A. V., Mozer, F. S., Hospodarsky, G., Bonnell, J., & Krasnoselskikh, V. (2018). Synthetic empirical chorus wave model from combined van allen probes and cluster statistics. *Journal of Geophysical Research: Space Physics*, *123*(1), 297–314. https://doi.org/10.1002/2017JA024843

Albert, J. M. (2005). Evaluation of quasi-linear diffusion coefficients for whistler mode waves in a plasma with arbitrary density ratio. *Journal of Geophysical Research*, *110*(A3), A03218. https://doi.org/10.1029/2004JA010844

Allison, H. J., Shprits, Y. Y., Zhelavskaya, I. S., Wang, D., & Smirnov, A. G. (2021). Gyroresonant wave-particle interactions with chorus waves during extreme depletions of plasma density in the Van Allen radiation belts. *Science Advances*, *7*(5), eabc0380. https://doi.org/10.1126/sciadv.abc0380

Artemyev, A., Agapitov, O., Breuillard, H., Krasnoselskikh, V., & Rolland, G. (2012). Electron pitch-angle diffusion in radiation belts: The effects of whistler wave oblique propagation. *Geophysical Research Letters*, *39*(8), L08105. https://doi.org/10.1029/2012GL051393

Baker, D. N., Blake, J. B., Callis, L. B., Cummings, J. R., Hovestadt, D., Kanekal, S., et al. (1994). Relativistic electron acceleration and decay time scales in the inner and outer radiation belts: Sampex. *Geophysical Research Letters*, *21*(6), 409–412. https://doi.org/10.1029/93GL03532

Baker, D. N., Kanekal, S. G., Horne, R. B., Meredith, N. P., & Glauert, S. A. (2007). Low-altitude measurements of 2–6 mev electron trapping lifetimes at $1.5 \leq L \leq 2.5$. *Geophysical Research Letters*, *34*(20), L20110. https://doi.org/10.1029/2007GL031007

Bortnik, J., Inan, U. S., & Bell, T. F. (2006). Landau damping and resultant unidirectional propagation of chorus waves. *Geophysical Research Letters*, *33*(3), L03102. https://doi.org/10.1029/2005GL024553

Bortnik, J., & Thorne, R. (2007). The dual role of elf/vlf chorus waves in the acceleration and precipitation of radiation belt electrons. *Journal of Atmospheric and Solar-Terrestrial Physics*, *69*(3), 378–386. https://doi.org/10.1016/j.jastp.2006.05.030

Breuillard, H., Zaliznyak, Y., Krasnoselskikh, V., Agapitov, O., Artemyev, A., & Rolland, G. (2012). Chorus wave-normal statistics in the Earth's radiation belts from ray tracing technique. *Annales Geophysicae*, *30*(8), 1223–1233. https://doi.org/10.5194/angeo-30-1223-2012

Carpenter, D. L., & Anderson, R. R. (1992). An ISEE/whistler model of equatorial electron density in the magnetosphere. *Journal of Geophysical Research*, *97*(A2), 1097–1108. https://doi.org/10.1029/91JA01548

Cattell, C., Wygant, J. R., Goetz, K., Kersten, K., Kellogg, P. J., von Rosenvinge, T., et al. (2008). Discovery of very large amplitude whistler-mode waves in earth's radiation belts. *Geophysical Research Letters*, *35*(1), L01105. https://doi.org/10.1029/2007GL032009

Chen, L., Thorne, R. M., Li, W., & Bortnik, J. (2013). Modeling the wave normal distribution of chorus waves. *Journal of Geophysical Research: Space Physics*, *118*(3), 1074–1088. https://doi.org/10.1029/2012JA018343

Glauert, S. A., & Horne, R. B. (2005). Calculation of pitch angle and energy diffusion coefficients with the PADIE code. *Journal of Geophysical Research*, *110*(A4), A04206. https://doi.org/10.1029/2004JA010851

Glauert, S. A., Horne, R. B., & Kirsch, P. (2021). Evaluation of SaRIF high-energy electron reconstructions and forecasts. *Space Weather*, *19*(12), e2021SW002822. https://doi.org/10.1029/2021SW002822

Glauert, S. A., Horne, R. B., & Meredith, N. P. (2014). Three-dimensional electron radiation belt simulations using the bas radiation belt model with new diffusion models for chorus, plasmaspheric hiss, and lightning-generated whistlers. *Journal of Geophysical Research: Space Physics*, *119*(1), 268–289. https://doi.org/10.1002/2013JA019281

Haque, N., Spasojevic, M., Santolík, O., & Inan, U. S. (2010). Wave normal angles of magnetospheric chorus emissions observed on the polar spacecraft. *Journal of Geophysical Research*, *115*(A4), A04202. https://doi.org/10.1029/2009JA014717

Hartley, D. P., Chen, L., Christopher, I. W., Kletzing, C. A., Santolik, O., Li, W., & Shi, R. (2022). The angular distribution of lower band chorus waves near plasmaspheric plumes. *Geophysical Research Letters*, *49*(9), e2022GL098710. https://doi.org/10.1029/2022GL098710

Hayakawa, M., Yamanaka, Y., Parrot, M., & Lefeuvre, F. (1984). The wave normals of magnetospheric chorus emissions observed on board geos 2. *Journal of Geophysical Research*, *89*(A5), 2811–2821. https://doi.org/10.1029/JA089iA05p02811

Horne, R. B., Kersten, T., Glauert, S. A., Meredith, N. P., Boscher, D., Sicard-Piet, A., et al. (2013). A new diffusion matrix for whistler mode chorus waves. *Journal of Geophysical Research: Space Physics*, *118*(10), 6302–6318. https://doi.org/10.1002/jgra.50594

Horne, R. B., Thorne, R. M., Glauert, S. A., Albert, J. M., Meredith, N. P., & Anderson, R. R. (2005). Timescale for radiation belt electron acceleration by whistler mode chorus waves. *Journal of Geophysical Research*, *110*(A3), A03225. https://doi.org/10.1029/2004JA010811

Horne, R. B., Thorne, R. M., Shprits, Y. Y., Meredith, N. P., Glauert, S. A., Smith, A. J., et al. (2005). Wave acceleration of electrons in the Van Allen radiation belts. *Nature*, *437*(7056), 227–230. https://doi.org/10.1038/nature03939

Kennel, C. F., Scarf, F. L., Fredricks, R. W., McGehee, J. H., & Coroniti, F. V. (1970). Vlf electric field observations in the magnetosphere. *Journal of Geophysical Research*, *75*(31), 6136–6152. https://doi.org/10.1029/JA075i031p06136

Kersten, T. (2016). *Electron acceleration and loss caused by wave-particle interactions in the Van Allen radiation belts*. British Antarctic Survey, Space Weather and Atmosphere Group. Retrieved from https://oro.open.ac.uk/47208/

Kletzing, C. A., Kurth, W. S., Acuna, M., MacDowall, R. J., Torbert, R. B., Averkamp, T., et al. (2013). The electric and magnetic field instrument suite and integrated science (EMFISIS) on RBSP. *Space Science Reviews*, *179*(1), 127–181. https://doi.org/10.1007/s11214-013-9993-6

Koons, H., & Roeder, J. (1990). A survey of equatorial magnetospheric wave activity between 5 and 8 RE. *Planetary and Space Science*, *38*(10), 1335–1341. https://doi.org/10.1016/0032-0633(90)90136-E

Koons, & Fennel, J. F. (2006). Space weather effects on communications satellites. *Science Bulletin International Union Radio Science*, *316*, 27–41.

Kurth, W. S., De Pascuale, S., Faden, J. B., Kletzing, C. A., Hospodarsky, G. B., Thaller, S., & Wygant, J. R. (2015). Electron densities inferred from plasma wave spectra obtained by the waves instrument on Van Allen probes. *Journal of Geophysical Research: Space Physics*, *120*(2), 904–914. https://doi.org/10.1002/2014JA020857

Lauben, D. S., Inan, U. S., Bell, T. F., & Gurnett, D. A. (2002). Source characteristics of elf/vlf chorus. *Journal of Geophysical Research*, *107*(A12), SMP10-1–SMP10-17. https://doi.org/10.1029/2000JA003019

Li, W., Bortnik, J., Thorne, R. M., Cully, C. M., Chen, L., Angelopoulos, V., et al. (2013). Characteristics of the Poynting flux and wave normal vectors of whistler-mode waves observed on themis. *Journal of Geophysical Research: Space Physics*, *118*(4), 1461–1471. https://doi.org/10.1002/jgra.50176

Li, W., Ma, Q., Thorne, R. M., Bortnik, J., Kletzing, C. A., Kurth, W. S., et al. (2015). Statistical properties of plasmaspheric hiss derived from van allen probes data and their effects on radiation belt electron dynamics. *Journal of Geophysical Research: Space Physics*, *120*(5), 3393–3405. https://doi.org/10.1002/2015JA021048

Li, W., Santolik, O., Bortnik, J., Thorne, R. M., Kletzing, C. A., Kurth, W. S., & Hospodarsky, G. B. (2016). New chorus wave properties near the equator from van allen probes wave observations. *Geophysical Research Letters*, *43*(10), 4725–4735. https://doi.org/10.1002/2016GL068780

Li, W., Thorne, R. M., Angelopoulos, V., Bortnik, J., Cully, C. M., Ni, B., et al. (2009). Global distribution of whistler-mode chorus waves observed on the themis spacecraft. *Geophysical Research Letters*, *36*(9), A00C14. https://doi.org/10.1029/2009GL037595

Li, W., Thorne, R. M., Bortnik, J., Nishimura, Y., Angelopoulos, V., Chen, L., et al. (2010). Global distributions of suprathermal electrons observed on themis and potential mechanisms for access into the plasmasphere. *Journal of Geophysical Research*, *115*(A12), A00J10. https://doi.org/10.1029/2010JA015687

Li, W., Thorne, R. M., Bortnik, J., Tao, X., & Angelopoulos, V. (2012). Characteristics of hiss-like and discrete whistler-mode emissions. *Geophysical Research Letters*, *39*(18), L18106. https://doi.org/10.1029/2012GL053206

Lorentzen, K. R., Blake, J. B., Inan, U. S., & Bortnik, J. (2001). Observations of relativistic electron microbursts in association with vlf chorus. *Journal of Geophysical Research*, *106*(A4), 6017–6027. https://doi.org/10.1029/2000JA003018

Lyons, L. R. (1974). Pitch angle and energy diffusion coefficients from resonant interactions with ion–cyclotron and whistler waves. *Journal of Plasma Physics*, *12*(3), 417–432. https://doi.org/10.1017/S002237780002537X

Malaspina, D. M., Jaynes, A. N., Hospodarsky, G., Bortnik, J., Ergun, R. E., & Wygant, J. (2017). Statistical properties of low-frequency plasmaspheric hiss. *Journal of Geophysical Research: Space Physics*, *122*(8), 8340–8352. https://doi.org/10.1002/2017JA024328

Mauk, B. H., Fox, N. J., Kanekal, S. G., Kessel, R. L., Sibeck, D. G., & Ukhorskiy, A. (2013). Science objectives and rationale for the radiation belt storm probes mission. *Space Science Reviews*, *179*(1), 3–27. https://doi.org/10.1007/s11214-012-9908-y

Meredith, N. P., Horne, R. B., & Anderson, R. R. (2001). Substorm dependence of chorus amplitudes: Implications for the acceleration of electrons to relativistic energies. *Journal of Geophysical Research*, *106*(A7), 13165–13178. https://doi.org/10.1029/2000JA900156

Meredith, N. P., Horne, R. B., Li, W., Thorne, R. M., & Sicard-Piet, A. (2014). Global model of low-frequency chorus (flhr < f < 0.1fce) from multiple satellite observations. *Geophysical Research Letters*, *41*(2), 280–286. https://doi.org/10.1002/2013GL059050

Meredith, N. P., Horne, R. B., Shen, X.-C., Li, W., & Bortnik, J. (2020). Global model of whistler mode chorus in the near-equatorial region ($|\lambda_m| < 18°$). *Geophysical Research Letters*, *47*(11), e2020GL087311. https://doi.org/10.1029/2020GL087311

Meredith, N. P., Horne, R. B., Sicard-Piet, A., Boscher, D., Yearby, K. H., Li, W., & Thorne, R. M. (2012). Global model of lower band and upper band chorus from multiple satellite observations. *Journal of Geophysical Research*, *117*(A10), A10225. https://doi.org/10.1029/2012JA017978

Meredith, N. P., Horne, R. B., Thorne, R. M., Summers, D., & Anderson, R. R. (2004). Substorm dependence of plasmaspheric hiss. *Journal of Geophysical Research*, *109*(A6), 1250. https://doi.org/10.1029/2004JA010387

Miyoshi, Y., Kataoka, R., Kasahara, Y., Kumamoto, A., Nagai, T., & Thomsen, M. F. (2013). High-speed solar wind with southward interplanetary magnetic field causes relativistic electron flux enhancement of the outer radiation belt via enhanced condition of whistler waves. *Geophysical Research Letters*, *40*(17), 4520–4525. https://doi.org/10.1002/grl.50916

Miyoshi, Y., Oyama, S., Saito, S., Kurita, S., Fujiwara, H., Kataoka, R., et al. (2015). Energetic electron precipitation associated with pulsating aurora: Eiscat and Van Allen probe observations. *Journal of Geophysical Research: Space Physics*, *120*(4), 2754–2766. https://doi.org/10.1002/2014JA020690

Mourenas, D., Artemyev, A. V., Agapitov, O. V., & Krasnoselskikh, V. (2014). Consequences of geomagnetic activity on energization and loss of radiation belt electrons by oblique chorus waves. *Journal of Geophysical Research: Space Physics*, *119*(4), 2775–2796. https://doi.org/10.1002/2013JA019674

Mourenas, D., Artemyev, A. V., Ripoll, J.-F., Agapitov, O. V., & Krasnoselskikh, V. V. (2012). Timescales for electron quasi-linear diffusion by parallel and oblique lower-band chorus waves. *Journal of Geophysical Research*, *117*(A6), A06234. https://doi.org/10.1029/2012JA017717

Olson, W., & Pfitzer, K. (1977). *Magnetospheric magnetic field modeling. Annual scientific report*. Air Force Office of Science Research.

Omura, Y., Katoh, Y., & Summers, D. (2008). Theory and simulation of the generation of whistler-mode chorus. *Journal of Geophysical Research*, *113*(A4), A04223. https://doi.org/10.1029/2007JA012622

Ozhogin, P., Tu, J., Song, P., & Reinisch, B. W. (2012). Field-aligned distribution of the plasmaspheric electron density: An empirical model derived from the IMAGE RPI measurements. *Journal of Geophysical Research*, *117*(A6), A06233. https://doi.org/10.1029/2011JA017330

Platino, M., Inan, U. S., Bell, T. F., Gurnett, D. A., Pickett, J. S., Canu, P., & Décréau, P. M. E. (2005). Whistlers observed by the cluster spacecraft outside the plasmasphere. *Journal of Geophysical Research*, *110*(A3), 3212. https://doi.org/10.1029/2004JA010730

Ross, J. P. J., Glauert, S. A., Horne, R. B., Watt, C. E., Meredith, N. P., & Woodfield, E. E. (2020). A new approach to constructing models of electron diffusion by emic waves in the radiation belts. *Geophysical Research Letters*, *47*(20), e2020GL088976. https://doi.org/10.1029/2020GL088976

Ross, J. P. J., Glauert, S. A., Horne, R. B., Watt, C. E. J., & Meredith, N. P. (2021). On the variability of emic waves and the consequences for the relativistic electron radiation belt population. *Journal of Geophysical Research: Space Physics*, *126*(12), e2021JA029754. https://doi.org/10.1029/2021JA029754

Santolík, O., Gurnett, D. A., Pickett, J. S., Chum, J., & Cornilleau-Wehrlin, N. (2009). Oblique propagation of whistler mode waves in the chorus source region. *Journal of Geophysical Research*, *114*(A12), A00F03. https://doi.org/10.1029/2009JA014586

Santolík, O., Němec, F., Gereová, K., Macúšová, E., de Conchy, Y., & Cornilleau-Wehrlin, N. (2004). Systematic analysis of equatorial noise below the lower hybrid frequency. *Annales Geophysicae*, *22*(7), 2587–2595. https://doi.org/10.5194/angeo-22-2587-2004

Santolik, O., Parrot, M., & Lefeuvre, F. (2003). Singular value decomposition methods for wave propagation analysis. *Radio Science*, *38*(1), 1010. https://doi.org/10.1029/2000RS002523

Shprits, Y. Y., & Ni, B. (2009). Dependence of the quasi-linear scattering rates on the wave normal distribution of chorus waves. *Journal of Geophysical Research*, *114*(A11), A11205. https://doi.org/10.1029/2009JA014223

Summers, D., Ni, B., Meredith, N. P., Horne, R. B., Thorne, R. M., Moldwin, M. B., & Anderson, R. R. (2008). Electron scattering by whistler-mode ELF hiss in plasmaspheric plumes. *Journal of Geophysical Research*, *113*(A4), A04219. https://doi.org/10.1029/2007JA012678

Taubenschuss, U., Khotyaintsev, Y. V., Santolík, O., Vaivads, A., Cully, C. M., Contel, O. L., & Angelopoulos, V. (2014). Wave normal angles of whistler mode chorus rising and falling tones. *Journal of Geophysical Research: Space Physics*, *119*(12), 9567–9578. https://doi.org/10.1002/2014JA020575

Thorne, R. M. (2010). Radiation belt dynamics: The importance of wave-particle interactions. *Geophysical Research Letters*, *37*(22), L22107. https://doi.org/10.1029/2010GL044990

Thorne, R. M., Li, W., Ni, B., Ma, Q., Bortnik, J., Chen, L., et al. (2013). Rapid local acceleration of relativistic radiation-belt electrons by magnetospheric chorus. *Nature*, *504*(7480), 411–414. https://doi.org/10.1038/nature12889

Thorne, R. M., O'Brien, T. P., Shprits, Y. Y., Summers, D., & Horne, R. B. (2005). Timescale for mev electron microburst loss during geomagnetic storms. *Journal of Geophysical Research*, *110*(A9), A09202. https://doi.org/10.1029/2004JA010882

Thorne, R. M., Smith, E. J., Burton, R. K., & Holzer, R. E. (1973). Plasmaspheric hiss. *Journal of Geophysical Research*, *78*(10), 1581–1596. https://doi.org/10.1029/JA078i010p01581

Tsurutani, B. T., & Smith, E. J. (1977). Two types of magnetospheric elf chorus and their substorm dependences. *Journal of Geophysical Research*, *82*(32), 5112–5128. https://doi.org/10.1029/JA082i032p05112

Tsyganenko, N. A., & Sitnov, M. I. (2005). Modeling the dynamics of the inner magnetosphere during strong geomagnetic storms. *Journal of Geophysical Research*, *110*(A3), 1108. https://doi.org/10.1029/2004JA010798

Tu, W., Cunningham, G. S., Chen, Y., Morley, S. K., Reeves, G. D., Blake, J. B., et al. (2014). Event-specific chorus wave and electron seed population models in DREAM3D using the Van Allen probes. *Geophysical Research Letters*, *41*(5), 1359–1366. https://doi.org/10.1002/2013GL058819

Van Allen, J. A. (1959). The geomagnetically trapped corpuscular radiation. *Journal of Geophysical Research*, *64*(11), 1683–1689. https://doi.org/10.1029/JZ064i011p01683

Van Allen, J. A., & Frank, L. A. (1959). Radiation around the earth to a radial distance of 107,400 km. *Nature*, *183*(4659), 430–434. https://doi.org/10.1038/183430a0

Wang, D., & Shprits, Y. Y. (2019). On how high-latitude chorus waves tip the balance between acceleration and loss of relativistic electrons. *Geophysical Research Letters*, *46*(14), 7945–7954. https://doi.org/10.1029/2019GL082681

Watt, C. E. J., Allison, H. J., Meredith, N. P., Thompson, R. L., Bentley, S. N., Rae, I. J., et al. (2019). Variability of quasilinear diffusion coefficients for plasmaspheric hiss. *Journal of Geophysical Research: Space Physics*, *124*(11), 8488–8506. https://doi.org/10.1029/2018JA026401

Wong, J.-M., Meredith, N. P., Horne, R. B., Glauert, S. A., & Ross, J. P. J. (2022). Electron diffusion by magnetosonic waves in the earth's radiation belts. *Journal of Geophysical Research: Space Physics*, *127*(4), e2021JA030196. https://doi.org/10.1029/2021ja030196